Extreme Glacier Melt on the Central Tibetan Plateau during the Summer of 2022: Detection and Mechanisms

Fei Zhu[1,2], Meilin Zhu[3]*, Lu An[1,2]

[1]College of Surveying and Geo-Informatics, Tongji University, Shanghai, 200092, China.

[2]Center for Spatial Information Science and Sustainable Development, Tongji University, Shanghai, 200092, China.

[3]Center for the Pan-Third Pole Environment, Lanzhou University, Lanzhou 730000, China.

Corresponding author: Meilin Zhu* (zhuml@lzu.edu.cn)

Abstract

Extreme glacier melt events accelerate mass loss, increase glacier instability, and temporarily increase downstream runoff, potentially alleviating drought conditions. Yet the glacier energy-mass balance in the Geladandong region—the headwater of both the Yangtze River (China's longest river) and Siling Co (Tibet's largest lake)—and its connection to the unprecedented 2022 summer melt remain insufficiently quantified. To address this gap, we integrated in situ mass balance observations and glacio-meteorological data from a 5,700 m monitoring site with an energy-mass balance model and applied a novel dual-threshold framework (based on mean and standard deviation) to identify extreme mass loss/melt events in short-term glacier mass balance records. Our novel methodology identified 2021/22 as a period of extreme mass loss and melt intensity, with melt during the 2022 summer heatwave reaching unprecedented extremes. These heatwaves caused an increase in melt amount of 317.8 mm w.e., amounting to 1.66 and 1.69 times the values recorded for the same period in 2019/20 and 2020/21, respectively. This extreme melt was driven by energy balance anomalies over the glacier surface, including reduced albedo, increased incoming longwave radiation, and enhanced sensible heat fluxes, processes that were strongly linked to persistent high temperatures. Such anomalies were driven by large-scale atmospheric circulation patterns, specifically the concurrent intensification and westward expansion of the Western Pacific Subtropical High, the eastward extension of the South Asian High, and the northward shift of the westerly circulation. This study proposes a framework for identifying extreme mass loss events in short-term glacier mass balance records and provides insights into glacier mass balance responses to extreme weather and climate events.

Keywords: Energy and mass balance, Extreme heat waves, Extreme melt, Extreme mass loss

1. Introduction

Extreme glacier melt events directly reflect glacier mass balance responses to extreme weather and climate events, such as heatwaves and droughts (Zhu et al., 2024a; Xu et al., 2024; Zhu et al., 2026b; Van Tiel et al., 2026). Across the Tibetan Plateau (TP) and surrounding regions, evidence from Xiao Dongkemadi Glacier, which holds the longest mass balance record in the central TP with observations since 1989, indicates that extreme mass loss events have been concentrated in 2000–2022, compared to 1989–2000 (Yao et al., 2012; Zhu et al., 2026a). In recent decades, scientific focus has increased on understanding spatiotemporal patterns and driving mechanisms of glacial retreat and thinning across TP (Bolch et al., 2012; Yao et al., 2012; Brun et al., 2017; Bhattacharya et al., 2021; Hugonnet et al., 2021). Studies have systematically revealed how atmospheric circulation patterns and dominant climate variables govern spatiotemporal variations in glacier mass balance across TP. Large-scale atmospheric anomalies generate distinct regional disparities in air temperature-precipitation regimes, potentially explaining the observed spatial heterogeneities in glacier mass balance (Yao et al., 2012, 2022). Meteorological controls exhibit strong regional differences: annual precipitation dominates mass balance variability in northwestern TP glaciers, whereas ablation-season air temperatures primarily regulate mass balance in southeastern regions (Zhu et al., 2018). Monsoon-driven cloud cover significantly influences summer surface energy budgets, as evidenced by detailed observations at East Rongbuk Glacier on the northern slopes of Mount Everest (Liu et al., 2021). These findings collectively demonstrate pronounced spatial heterogeneity in the sensitivity of TP glaciers to climate forcing. However, understanding the mechanisms underlying extreme mass loss events across TP and adjacent regions remains inadequate.

Emerging evidence identifies compound heat-drought events as primary drivers of extreme glacier mass loss. Regional case studies across cryosphere hotspots—including the eastern Tien Shan (Xu et al., 2024), Qilian Mountains (Chen et al., 2024), and Tanggula and Nyainqêntanglha ranges (Zhu et al., 2024a)—reveal unprecedented mass loss rates associated with atmospheric teleconnections and glacier surface energy

budget anomalies. These events typically result from synergistic interactions between external forcing (heat extremes/precipitation deficits) and intrinsic glacier responses (albedo feedback/turbulent heat flux anomalies). When superimposed, these drivers can push glacier systems beyond equilibrium thresholds within weeks, producing nonlinear mass losses that challenge conventional model predictions. However, comprehensive event attribution remains challenging across most of TP.

This knowledge gap stems from two critical limitations: (1) methodological constraints in detecting extremes from short mass balance records (under ten years), and (2) sparse in situ monitoring networks—fewer than ten TP glaciers have decadal-scale measurements. Traditional extreme detection methods (e.g., 10th percentile thresholds, generalized extreme value distributions) require multi-decadal data unavailable for over 90% of TP glaciers. Consequently, developing and testing frameworks, such as the dual-threshold approach proposed in this study, for identifying extremes from short-term observations (under ten years) are essential for advancing glacier research in this region.

The exceptional 2022 heatwave, characterized by unprecedented air temperature anomalies and precipitation deficits, served as an ideal natural experiment to address these challenges. Researchers have systematically analyzed the temporal characteristics (frequency/duration), intensity metrics, and hydrological impacts of the 2022 heatwave-drought events in both the Yangtze River Basin (Hua et al., 2023; Jeong et al., 2023) and TP (Yan et al., 2024; Zhou et al., 2024). Hua et al. (2023) demonstrated that a 6.45 °C temperature anomaly, observed in central China over the 21-day period from 6 to 26 August 2022, broke historical records and established a new threshold for defining future record-breaking daily maximum temperatures in the region. During summer 2022, central-eastern TP recorded mean maximum air temperatures 3.5 °C above the 1961–2013 baseline (Zhou et al., 2024). Concurrently, central-eastern TP precipitation was 2.4 σ below the 1961–2013 mean (Zhou et al., 2024), while southern China experienced rainfall deficits of 2–3 $mm \cdot day^{-1}$ (Jeong et al., 2023). Multiple drivers have been identified, including synoptic-scale circulation anomalies (Hua et al., 2023; Duan et al., 2024), Indian Ocean Dipole–La Niña interactions (Jeong et al., 2023),

land-atmosphere feedback (Li et al., 2023), and localized energy budget perturbations (Tian et al., 2023; Zhang et al., 2023). These studies collectively reveal that both TP and eastern China faced unprecedented extreme heat and precipitation deficits during summer 2022.

The key glaciated complexes most exposed to this extreme event are located in the Central Tanggula Mountains—a critical cryospheric zone in the central TP that encompasses the Geladandong and Dongkemadi regions and the Puruogangri Ice Cap. These glaciers provide a unique opportunity to develop novel methodologies for identifying extreme mass loss events and elucidating their driving mechanisms. Continuous mass balance monitoring began in 1989 at Xiao Dongkemadi Glacier in the Dongkemadi region (Pu et al., 2008; Yao et al., 2012). Since entering a negative mass balance regime around 1995, Xiao Dongkemadi Glacier has experienced accelerated mass loss at ~−0.3 m w.e. yr^{-1} since 2000 (Pu et al., 2008; Yao et al., 2012; Kang et al., 2015). Research demonstrates that summer mass balance controls annual mass balance variations in summer-accumulation-type glaciers in the Dongkemadi region (Liang et al., 2018). The Geladandong region recorded glacier mass loss rates of −0.24 ± 0.08 m w.e. yr^{-1} from the 1960s to 2018 (King et al., 2023).

Sangqu Glacier, located south of Geladandong, was selected for in situ glacio-meteorological observations. Meltwater from Sangqu Glacier drains into Siling Co, the largest lake in Tibet. Therefore, investigating extreme melt events in this region will improve the understanding of glacier change patterns. Hence, this study aims to (i) investigate the energy-mass balance characteristics of Sangqu Glacier; (ii) develop a novel framework for detecting extreme mass loss events in short-term glacier mass balance records; and (iii) elucidate melting mechanisms driven by the unprecedented 2022 summer heatwaves. By integrating multi-source observational data with an energy-mass balance model, this work advances understanding of glacier responses to extreme heatwaves and proposes an innovative statistical dual-threshold framework as a methodological advancement for addressing critical gaps in TP cryosphere research.

2. Study Area

The valley-type continental Sangqu Glacier in Geladandong was selected as the study site (Fig. 1). This south-facing glacier has a length of 2.2 km and covers 18 km², and spans an elevational range of 5,400–6,104 m a.s.l.. Situated in central TP, the region experiences low air temperatures and a semi-arid continental climate. Over 70% of annual precipitation occurs during June–September, coinciding with the warmest season (Zhu et al., 2024a). Glacier ablation and accumulation in Geladandong primarily occur from June to September, characterized by a short melt season (Pu et al., 2008). Multi-temporal digital elevation model differencing and in situ stake measurements reveal continuous mass loss in this region since the 1990s (Yao et al., 2012; King et al., 2023). Based on the combined in situ and ERA5-corrected precipitation data, the mean annual precipitation at the Sangqu Glacier site was 510.5 mm for the period October 2019--September 2022. Geodetic mass balance estimates from Dussaillant et al. (2025) indicate that Sangqu Glacier lost ~515.4 mm w.e. yr^{-1} over the period 1957–2024, consistent with the regional mass loss pattern. Moreover, Sangqu Glacier lies at the northern limit of Indian monsoon influence (Tian et al., 2001; Yao et al., 2013). Based on the observed ice temperatures and the presence of meltwater percolation and refreezing in the ablation zone, Sangqu Glacier is polythermal, with cold ice in the upper accumulation zone and temperate ice in the ablation zone. This thermal regime is consistent with observations on neighboring glaciers on the central TP, such as Xiao Dongkemadi Glacier (Fig.1b), where superimposed ice formation plays a significant role in the mass balance (Fujita et al., 1996).

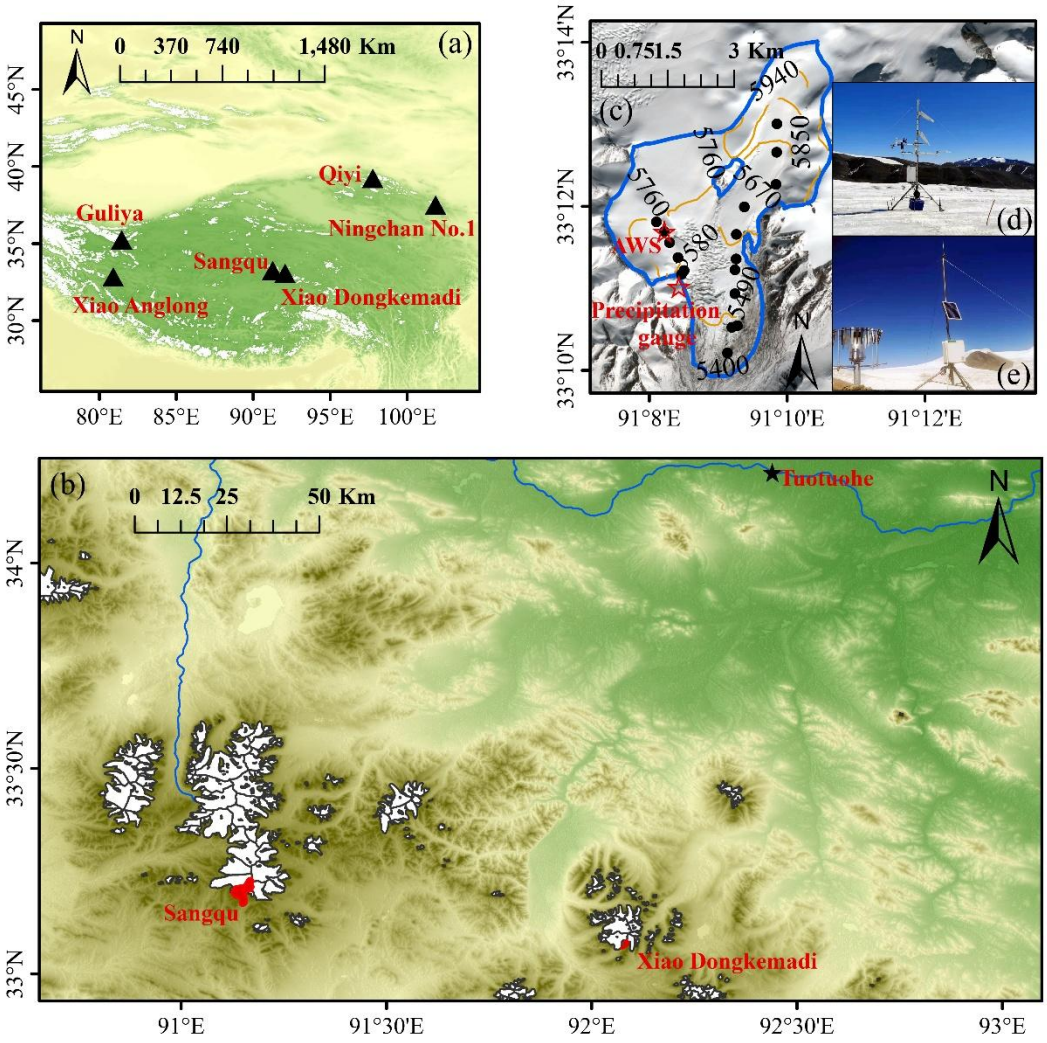


Figure 1. Overview of the study area. (a, b) Geographical location of the glacier on the TP: (a) regional context; (b) enlarged local map. (c) Sentinel-2 image (2022-12-05) with contour lines showing the topography of Sangqu Glacier. (d, e) Photographs of the AWS and the precipitation gauge on Sangqu Glacier (Photo credit: Fei Zhu). The positions of the AWS, precipitation gauge, and stakes are indicated in panel (c).

3. Data

3.1 Meteorological Data on Glacier Surface

An automatic weather station (AWS) was installed on Sangqu Glacier at 5,700 m a.s.l. in October 2020 (Fig. 1c and 1d). Hourly measurements included air temperature, relative humidity, wind speed, incoming/outgoing shortwave radiation, and incoming/outgoing longwave radiation. Air temperature and relative humidity probes, along with wind speed, were mounted 2 m above the glacier surface. Radiation sensors

were installed more than 1.6 m above the surface. Data from July 2021 were incomplete due to power failure; operations resumed on 13 July 2021. A Geonor T-200B precipitation gauge, equipped with a double-alter shield to minimize wind-induced undercatch, was installed on adjacent bedrock (5,665 m a.s.l.) to record precipitation at 30-min intervals (Fig. 1e). Meteorological data cover the period October 2020 to July 2022. As the observational data only cover the period up to July 2022, the meteorological forcing for August–September 2022 was reconstructed using ERA5 reanalysis data (see Sect. 4.1).

3.2 Glacier Mass Balance Data

Glacier mass balance measurements began in October 2019 using stake and snow-pit methods. Stakes were distributed between 5,400 and 5,750 m a.s.l. (Fig. 1c). Stake heights and snow-pit characteristics were measured in October 2019, October 2020, October 2021, and July 2022. Using these measurements and assumed densities (snow: 300 kg m^{-3}; ice: 900 kg m^{-3}), mass balance data were derived for three periods: October 2019–October 2020, Octosber 2020–October 2021, and October 2021–July 2022. Point and mass balances were calculated following Yao et al. (2012), and glacier-wide mass balances were obtained by integrating these point measurements over the glacier area using an elevation-based interpolation method.

3.3 Other Data

Hourly ERA5 reanalysis data (Hoffmann et al., 2019), including air temperature, precipitation, relative humidity, wind speed, and incoming shortwave radiation, were used. Additionally, variables at the 500, 200, and 300 hPa pressure levels, including geopotential height, horizontal wind, temperature, and specific humidity, were also employed in this study. These data were used to reconstruct meteorological conditions at the AWS locations and to analyze the characteristics and underlying causes of the extreme melt. Glacier boundaries were obtained from the Second Chinese Glacier Inventory (Guo et al., 2015). The 90-m resolution Shuttle Radar Topography Mission (SRTM) digital elevation model (DEM) was used to extract elevation, slope, and aspect. These data also drove model calculations of top-of-atmosphere radiation (Hock and Holmgren, 2005).

4. Methods

4.1 Energy and Mass Balance Model

We established the distributed coupled energy balance–snow/firn model (EBFM) and subsurface model for Sangqu Glacier. This model describes the evolution of vertical temperature, density, and water content profiles within the snow/ice pack, incorporating percolation and refreezing processes (Van Pelt et al., 2012). The EBFM has been successfully applied to mountain glaciers, including Abramov Glacier in the Pamir Alay (Kronenberg et al., 2022) and Kuoqionggangri Glacier in the Nyainqêntanglha Mountains (Zhu et al., 2024b). Detailed model descriptions are provided by Van Pelt et al. (2012, 2019). The sum of each surface energy component is equal to the melt energy (Q_M) and the surface energy balance formula is as follows (Van Pelt et al., 2012):

$$Q_M = S_{net} + l_{net} + Q_H + Q_L + Q_G \quad (1)$$

S_{net} is the net shortwave radiation, which consists of the incoming (S_{in}) and outgoing (S_{out}) shortwave radiation. The S_{out} depends on the albedo of the glacier surface. L_{net} is the difference between the incoming (L_{in}) and the outgoing longwave radiation (L_{out}). Q_H and Q_L are the sensible and latent heat fluxes, respectively. Q_G represents the snow and ice heat flux. The subsurface heat flux Q_G in EBFM is computed by solving the one-dimensional heat conduction equation. Following established approaches for polythermal glaciers (Van Pelt et al., 2012), the effective thermal conductivity is parameterized as a function of snow/firn/ice density based on Ostin and Andersson (1991) and Sturm et al. (1997). The heat capacity is treated as a function of temperature following Yen (1981). Following micrometeorological convention, energy fluxes directed towards the surface are positive. The dichotomous iterative method was used to calculate the glacier's surface temperature, and the surface temperature was constrained at less than 0°C.

The glacier mass balance on TP comprises four primary processes: snowfall, melting, sublimation/evaporation, and refreezing. The glacier mass balance at each grid point can be expressed as:

$$B = P - M - E_{eva/sub} + C_r \quad (2)$$

B denotes the point mass balance of each grid. P is for precipitation. M is the amount of melt on glacier surface. $E_{\mathrm{eva/sub}}$ refers to the sublimation and evaporation. C_{r} is for refreezing. Surface ablation involves melting, sublimation and evaporation. In this study, sublimation and evaporation were quantified based on latent heat flux and surface temperature. Specifically, the phase transition criteria were defined as follows: sublimation was identified under conditions where surface temperatures remained below the melting point while latent heat flux exhibited negative values. Conversely, evaporation was classified when surface temperatures exceeded the melting point with concurrent negative latent heat flux values. Additionally, the model explicitly includes deposition and condensation processes, which are strictly governed by positive latent heat flux conditions. Here, deposition occurs when surface temperatures remain below the melting point with positive latent heat flux, while condensation occurs when surface temperatures exceed the melting point with positive latent heat flux. However, both processes were excluded from the final analysis due to their negligible impact on the overall mass balance. Mass accumulation comprises snowfall and refreezing processes. Specifically, surface accumulation was derived from solid precipitation events, determined by a temperature-dependent rain-snow transition threshold applied to atmospheric forcing data. Subsurface liquid water sources, including meltwater, rainfall, and condensation, were tracked as potential contributors to refreezing.

In this study, the EBFM was applied as a distributed model at a spatial resolution of 100 m and hourly temporal resolution, driven by air temperature, relative humidity, wind speed, total precipitation, and cloud fraction from October 2019 to September 2022. As the AWS was installed in October 2020, one year later than the start of mass balance observations (October 2019), and observations were only available through July 2022, meteorological forcing for October 2019–October 2020 and for August–September 2022 was reconstructed. To obtain the air temperature, relative humidity, wind speed, total precipitation, and cloud fraction at hourly intervals from October 2019 to October 2022, meteorological data were reconstructed at hourly intervals using the

Random Forest method by combining the air temperature, relative humidity, wind speed, and S_{in} measured at AWS and ERA5. This study applied the Random Forest method for statistical downscaling of ERA5 reanalysis data to reconstruct near-surface meteorological variables, specifically air temperature, relative humidity, wind speed, and S_{in} at a glacier surface AWS site.

Observational data from an AWS were first spatially and temporally matched with ERA5 grid points to construct training and testing datasets. Predictor variables included surface variables (2 m air temperature, dewpoint temperature, 10 m wind components, and surface pressure) and at 300 hPa and 500 hPa (temperature, humidity, wind components, and geopotential height), from which derived variables such as wind speed and relative humidity were also computed. To minimize overfitting and obtain robust estimates of model performance, we applied three repetitions of five-fold cross-validation, where the training data were repeatedly split into five subsets, each serving in turn as the validation set. Evaluation results indicate that the Random Forest model achieves high predictive accuracy. Comparisons between the downscaled estimates and in-situ observations yielded R^2 (coefficient of determination) values of 0.99, 0.96, 0.94, and 0.96 for air temperature, relative humidity, wind speed, and S_{in}, respectively, at the hourly scale (Fig. S1), with similarly robust performance during the ablation season (June–September) (Fig. S8).

The cloud fraction was defined as the ratio of incoming shortwave radiation to total radiation at the top of the atmosphere. The hourly calculation of S_{TOA} (total radiation from the top of the atmosphere) was based on elevation, slope, and aspect parameters (Hock & Holmgren, 2005). We also estimated the total precipitation on Sangqu Glacier from October 2019 to September 2022. This was achieved by combining total precipitation data from ERA5 with data from direct measurements. First, we calculated the ratio of total measured precipitation to that estimated by ERA5 for the overlap period (October 2020 to July 2022). Then, the ratio was used to correct all reanalysis precipitation data from October 2019 to September 2021. This approach has been extensively utilized in glacier–related studies on TP (Zhu et al., 2024b).

The spatial interpolation of meteorological data considered the topographic

conditions (elevation, slope, and aspect) of Sangqu Glacier. The mean air temperature lapse rate was 0.6°C/1000 m. Precipitation gradient was the parameter for the EBFM model, considering glacier mass balance and albedo. Following the approach of Hock and Holmgren (2005) in their distributed surface energy-balance modeling for Storglaciären, Sweden, the wind speed and relative humidity measured at the single AWS are assumed to be representative of the entire glacier, due to the limited availability of spatially distributed observations and the relatively small spatial variability in relative humidity across the glacier.

The methodology for calculating the energy balance components at the glacier surface was based on the findings of previous studies. The S_{in} was calculated following Klok and Oerlemans (2002) and Van Pelt et al. (2012) and accounts for the grid aspect and shading by the surrounding terrain. S_{out} depends on surface albedo. Snow albedo was related to temperature and humidity (Oerlemans and Knap, 1998; Bougamont et al., 2005; Van Pelt et al., 2019), and ice albedo was calculated using the dew point temperature Mölg et al. (2008). The L_{in} was calculated based on the relative humidity and air temperature (Brunt, 1932). L_{out} was calculated using the Stefan–Boltzmann law. The surface emissivity (ε) was set to 1.0 following Van Pelt et al. (2012). Q_H and Q_L were calculated using the method proposed by Klok and Oerlemans (2002). Q_G was obtained as the sum of the conductive heat fluxes (Reijmer and Hock, 2008; Van Pelt et al., 2012).

4.2 Modelling Validation and Uncertainty

To reduce uncertainties arising from manual parameter calibration, this study proposes a stepwise parameter calibration scheme. First, the Shuffled Complex Evolution (SCE-UA) algorithm (Duan et al., 1992) was employed to calibrate parameters related to incoming longwave radiation parameterization using RMSE as the objective function. Subsequently, for the EBFM model, the Nondominated Sorting Genetic Algorithm II (NSGA-II) multi-objective optimization algorithm (Deb et al., 2002) was applied. Utilizing daily-scale surface albedo data from on-glacier meteorological stations and glacier-wide mass balance observations, the EBFM parameters were calibrated with both the R^2 and RMSE as dual objective functions.

Following parameter calibration, the model's performance was rigorously validated using in-situ observational data to the greatest extent possible. Specifically, validation utilized in situ measurements of albedo, L_{in}, and L_{out} from an AWS installed on the glacier. Additionally, point-scale mass balance data across different elevations, along with glacier-wide mass balance records for the periods October 2019–October 2020, October 2020–October 2021, and October 2021–July 2022, were used to assess the simulation accuracy. To further evaluate the model's performance in simulating glacier mass balance, seasonal-scale glacier-wide mass balance data observed during 2020–2021 were also employed.

Fig 2 presents a comparison between measured and modelled albedo, L_{in}, and L_{out} at the AWS site. Albedo was directly derived as the ratio S_{out} / S_{in} at the AWS site. This observed albedo time series was used for model calibration and validation. Daily albedo simulations showed good agreement with observations, with an R of 0.76 and an RMSE of 0.1 (Fig. 2a). This agreement improved for 7-day average values (R = 0.74, RMSE = 0.09; Fig. S2). Simulations of L_{in} and L_{out} were also robust. Modelled L_{in} correlated well with measurements (R = 0.9, RMSE = 22 W m^{-2}; Fig. 2b), as did L_{out} (R = 0.95, RMSE = 11 W m^{-2}; Fig. 2c). The high accuracy in simulating radiation components supports reliable estimates of L_{net} and glacier surface temperature.

The performance of the EBFM model in simulating glacier mass balance was evaluated using multi-scale comparisons. At the point scale, the RMSE between simulated and observed mass balances was 288 mm w.e. (Fig. 2e). The R at the point scale is 0.90 (Fig. 2e). At the glacier-wide scale, the RMSE decreased to 101 mm w.e. (Figs. 3f and 3g). Moreover, the simulated cumulative mass balance from 1 October 2019 to 30 September 2022 closely matched observations (Fig. 3g). We also compared the differences between observed and simulated temperatures at 3 m and 5 m within the glacier, with correlation coefficients of 0.94 and 0.96, respectively (Fig. S3).

To assess model accuracy at seasonal resolution, we compared simulated and in situ mass balances for the 2020–2021 balance year, yielding an RMSE of 329 mm w.e. (Fig. 2d). We also compared our simulated 2021/22 mass balance for Sangqu Glacier with independent estimates. The simulated value (−919 mm w.e.) closely agreed with

in-situ observations from the neighbouring Xiao Dongkemadi Glacier (−881 mm w.e.; Zhu et al., 2026a), further confirming model consistency. In contrast, the satellite-derived product of Dussaillant et al. (2025) reported −1278 mm w.e. for Sangqu Glacier, which is more negative than our result (Fig. 2h). Despite this numerical difference, all independent lines of evidence, including our model, the in-situ data from Xiao Dongkemadi Glacier (Zhu et al., 2026a), and the global assessment of Dussaillant et al. (2025), suggest that 2021/22 was likely an extreme mass loss year for Sangqu Glacier.

Collectively, these multi-scale and cross-site comparisons demonstrate that the EBFM model provides reliable energy and mass balance simulations for Sangqu Glacier, thereby supporting its use for detailed analyses of energy and mass balance processes.

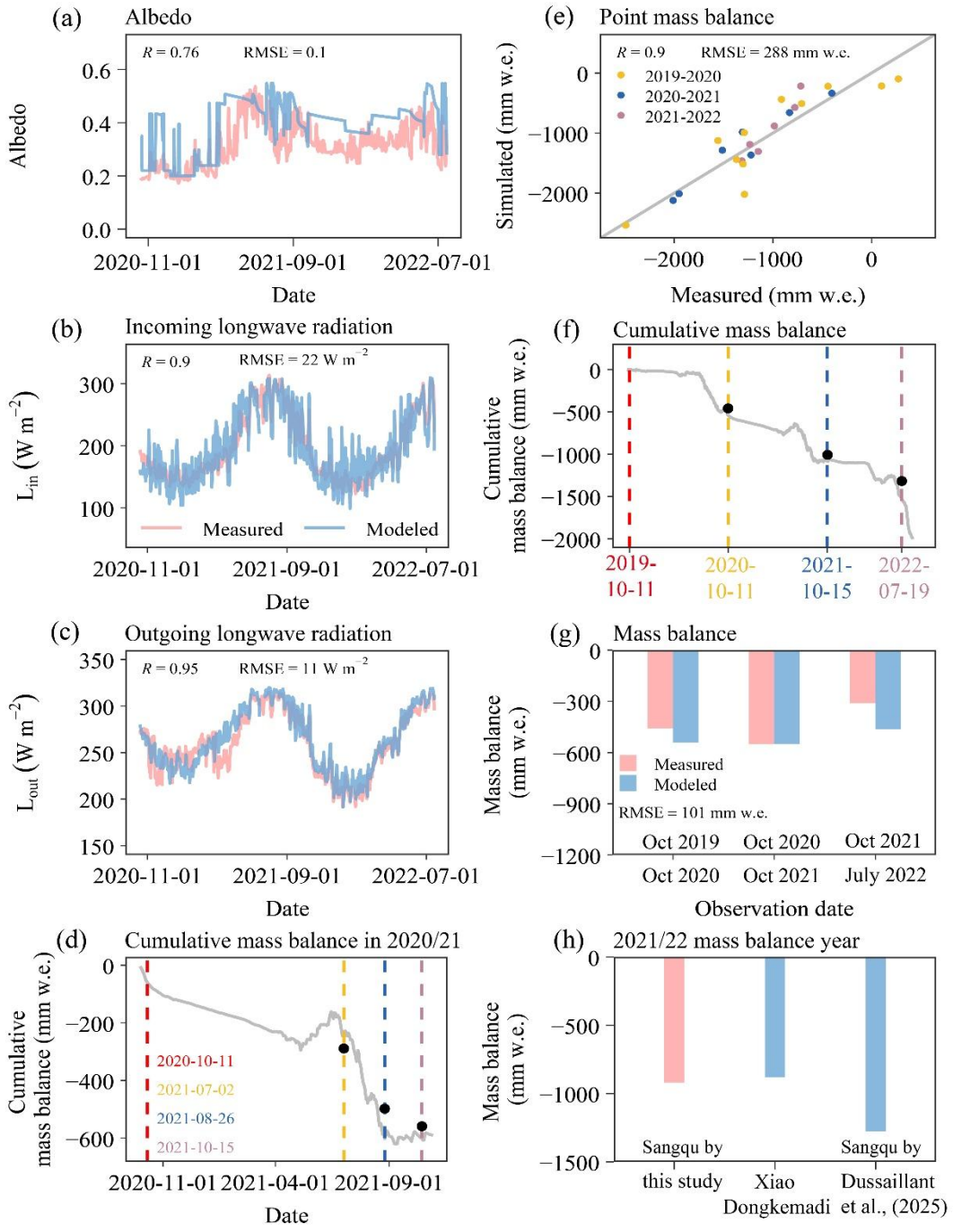


Figure 2. Comparison between observations and simulations of (a) albedo, (b) L_{in}, (c) L_{out}, (d) glacier mass balance from June to September 2021, (e) point mass balance at different elevations, (f) accumulation mass balance, and (g) glacier-wide mass balance for the periods 2019/20, 2020/21, and from October 2021 to July 2022. (h) Comparison of simulated glacier mass balance for Sangqu Glacier in 2021/22 with observed mass balance for Xiao Dongkemadi Glacier and with mass balance data for the same Sangqu Glacier derived from multi-source satellite remote sensing by Dussaillant et al. (2025).

This study conducts sensitivity and uncertainty tests based on the parameter selection framework proposed by Van Pelt et al. (2012). Model output uncertainty primarily originates from key parameters governing albedo (snow, firn, and ice), precipitation gradients, critical temperature thresholds (e.g., the rain-snow partitioning threshold), temperature lapse rate, parameters for downward shortwave radiation, and turbulent flux calculations, all of which are crucial determinants of mass balance simulation accuracy. Following the recommendation of Van Pelt et al. (2012), an uncertainty of ±0.03 was applied to the albedo of snow, ice, and firn, along with the relevant parameters. The aerosol transmissivity coefficient, a parameter influencing S_{in}, was perturbed by ±0.01. The temperature lapse rate was adjusted by ±0.1 °C /1000 m. All other parameters were perturbed by ±10% to assess sensitivity and associated uncertainty. The sensitivity was quantified using the formula provided below (Oerlemans et al., 1998):

$$\frac{dM}{dS} = \frac{M(S_H) - M(S_L)}{2} \tag{3}$$

M is the glacier-wide mass balance, and S represents the parameter for which sensitivity tests are to be performed.

The results of the sensitivity tests are presented in the supplementary materials (Tables S1-S4). The glacier-wide mass balance of the Sangqu Glacier exhibits particularly high sensitivity to ice and snow albedo. Specifically, the sensitivities to parameters related to snow, firn, and ice albedo are 123.2, 114.7, −0.3, and 126.3 mm w.e. a^{-1}, respectively. The temperature lapse rate shows a sensitivity of -141.4 mm w.e. a^{-1}. The background turbulent exchange coefficient and turbulent flux coefficient yield sensitivities of 8.3 and -55 mm w.e. a^{-1}, respectively. In comparison, the sensitivity of the glacier-wide mass balance to the rain-snow temperature threshold and precipitation gradient are relatively minor, at 0.5 and −2.2 mm w.e. a^{-1}, respectively. The sensitivity to the aerosol transmissivity coefficient is −20.2 mm w.e. a^{-1}. The glacier-wide annual mass balance has a sensitivity of −9.9 mm w.e. a^{-1} to effective thermal conductivity and +10.5 mm w.e. a^{-1} to heat capacity.

The total uncertainty in the modelled mass balance for each mass balance year was

estimated following the error propagation law described by Zhu et al. (2024a) and Zhu et al. (2021). The average uncertainty over three mass balance years is 264.3 mm w.e. (Tables S2-S4). A comprehensive sensitivity analysis of key model parameters during the heatwave period was conducted, and the associated uncertainty in melt amount was estimated to be 99.3 mm w.e. (Table S1).

4.3 Standardized heatwave index

The standardized heatwave index (S_{HI}) was employed to detect heatwave events (Raei et al., 2018; Shan et al., 2024). This index quantifies temperature deviations, ranking heatwaves by their probability of occurrence relative to a climatological reference period. As highlighted by Shan et al. (2024), the choice of this reference period is critical due to the non-stationarity of temperature records caused by global warming. Using the entire period of record can introduce bias, as the climate normal for a given day would be influenced by long-term trends rather than representing the recent expected conditions to which ecosystems and society may have adapted.

To address this, Shan et al. (2024) explicitly recommend using a dynamic, 30-year moving window to better account for climate non-stationarity. Following their methodology, we used the past 30 years as the historical reference period (1992-2021). For each target day, the 30-year mean of the accumulated temperature is calculated and used as the expected normal, allowing the index to reflect anomalies relative to a recent, locally adapting baseline. The S_{HI} for each day was then calculated as follows (Raei et al., 2018; Shan et al., 2024):

$$\hat{T}_{m,i} = \begin{cases} \dfrac{1}{N_h} \displaystyle\sum_{j=i-N_h+1}^{i} T_{m,j}, & \text{if } i \geq N_h \\ \dfrac{1}{N_h} \left(\displaystyle\sum_{j=365-N_h+i+1}^{365} T_{m-1,j} + \sum_{j=1}^{i} T_{m,j} \right), & \text{if } i < N_h; \end{cases} \tag{4}$$

$$S_{HI\,m,i} = \Phi^{-1}\left(F^{h}_{m,i}\left(\hat{T}_{m,i}\right)\right) \tag{5}$$

The variables i and j denote calendar days, with $i,j \in \{1, 2, \cdots, 365\}$;

$m \in \{1, 2, \cdots, M\}$ represents the year, M is the total number of years in the historical record. The daily mean temperature $T_{m,i}$ for day i of year m is used directly. For leap years, the mean temperatures of February 28 and February 29 are averaged and assigned to February 28, after which the leap day is excluded. The accumulation period for a heatwave is denoted by N_h, and $\hat{T}_{m,i}$ represents the mean temperature over the accumulation period ending on day i. The cumulative distribution function (CDF) $F^h_{m,i}$ is fitted to the set $\{\hat{T}_{m,i}, \hat{T}_{m-1,i}, \cdots, \hat{T}_{m-29,i}\}$ when $m \geq 30$; otherwise, it is fitted to $\{\hat{T}_{30,i}, \hat{T}_{29,i}, \cdots, \hat{T}_{1,i}\}$. The inverse of the standard normal CDF is denoted as Φ^{-1}, and $\mathrm{S}_{\mathrm{HI}m,i}$ is the resulting standardized heatwave index for day i of year m.

Fig 3 presents the identified heatwave events (Figs. 3a, 3c and 3e) and the associated air temperature anomaly magnitudes (Figs. 3b, 3d and 3f). The anomalies are calculated relative to the 1992–2021 climatology. The first dataset consists of in-situ observations from the Tuotuohe meteorological station, located approximately 150 km from Sangqu Glacier. This station has been widely employed in previous studies on glacier mass balance and hydrological processes in the region (Gao et al., 2012). Using daily mean air temperatures from this station, three heatwave events were identified: 1–9 June, 3–16 July, and 3–29 August (Figs. 3a and 3b). The second dataset is derived from the ERA5 reanalysis, specifically from the grid cell corresponding to the Tuotuohe meteorological station. Based on daily mean air temperatures extracted from this dataset, three heatwaves were identified: 1–8 June, 7–15 July, and 4 August–1 September (Figs. 3c and 3d). The third dataset is also from ERA5 reanalysis but represents the grid cell covering the study site, Sangqu Glacier. Analysis of daily mean air temperatures from this dataset revealed three heatwave periods: 1–10 June, 7–17 July, and 2 August–1 September (Figs. 3e and 3f).

To minimize uncertainties arising from the use of multiple data sources, only the overlapping periods consistently identified by all three datasets were defined as the final heatwave events (Fig. 3g). Accordingly, the three heatwave events in the summer of 2022 were delineated as 1–8 June, 7–15 July, and 4–29 August. Fig 3h shows that the

air temperature anomaly magnitudes on the Sangqu Glacier AWS during the summer heatwaves of 2022 were 4.9 °C, 1.6 °C, and 2 °C, respectively.

This approach, which integrates multi-source data consistency with a rigorous objective statistical method for defining event extremity and independence, effectively resolves discrepancies among different datasets and enhances the reliability of the heatwave identification.

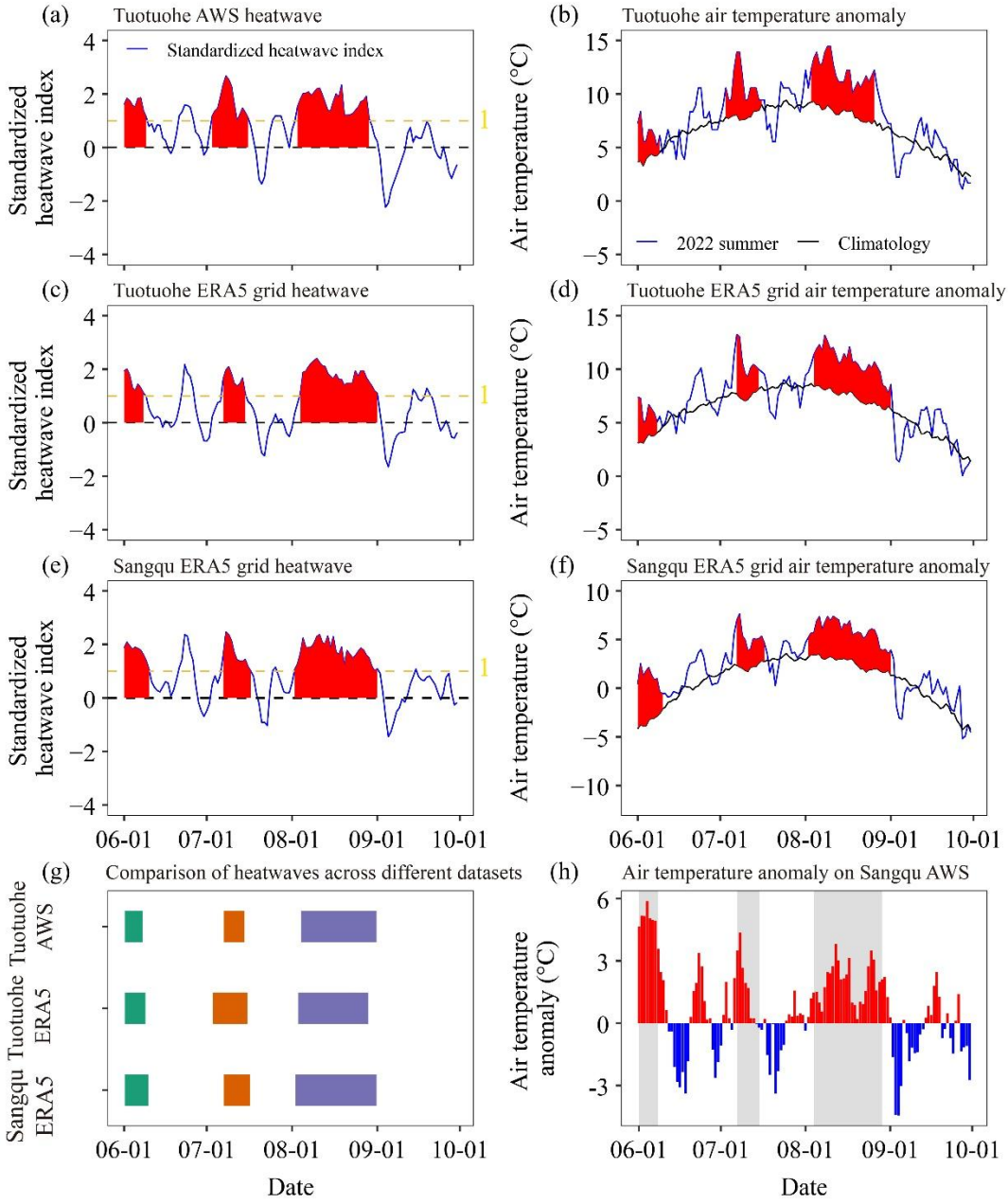


Figure 3. Identification of heatwave events from June to September 2022. Air temperature anomalies are calculated relative to the 1992–2021 climatology. (a, b) Heatwave events and

corresponding temperature anomalies at the Tuotuohe meteorological station. (c, d) As in (a, b), but for the ERA5 grid cell containing the Tuotuohe meteorological station. (e, f) As in (a, b), but for the ERA5 grid cell containing Sangqu Glacier. In panels (a), (c), and (e), the yellow line marks the standardized heatwave index threshold of 1; a heatwave is identified when the index exceeds this threshold for at least three consecutive days. (g) Comparison of heatwave events identified from the three datasets shown in (a), (c), and (e). (h) Summer (June–September) temperature anomalies at Sangqu Glacier in 2022 based on the identified heatwave events.

4.4 A Dual-Threshold Framework for Identifying Extreme Mass Loss Events in Short-Term Glacier Mass Balance Records

Conventional approaches for detecting extreme mass loss events, such as percentile thresholds (Vargo et al., 2020) and generalized extreme value (GEV) distributions (Thibert et al., 2018), typically require observational records exceeding 30 years. On the TP, however, most glacier mass balance series span less than a decade, with the sole exception of Xiao Dongkemadi Glacier (since 1989; Yao et al., 2012). To address this limitation, we developed a dual-threshold framework capable of reliably identifying extreme mass loss events from short-term records (<10 years).

The core idea is to establish a mathematical link between two approaches for defining extreme events within a training period: a percentile-based method and a method based on deviations from the mean. Let B_y denote the annual mass balance (mm w.e.). The available record is split into a training set (years T_{train}) and a test set (years T_{test}). The training set is used to calibrate the relationship between the two methods, and the calibrated rule is then applied to the test set.

First, we identify extreme years in the training set using a percentile-based threshold. With a default probability level $p = 0.10$ (the 10th percentile), the threshold Q_P is computed, and all years in the training set with annual mass balance below Q_P are defined as extreme mass loss events, denoted by the set Y_{target}.

Second, we calculate the mean μ and standard deviation σ of the annual mass balance in the training set:

$$\mu = \frac{1}{n}\sum_{i=1}^{n} B_i, \sigma = \sqrt{\frac{1}{n-1}\sum_{i=1}^{n}(B_i - \mu)^2} \quad (6)$$

n is the number of years in the training set, and B_i is the mass balance of the i-th training year.

Third, we determine a multiplier k such that the rule $B < \mu - k \cdot \sigma$ identifies the same extreme years as the percentile method. By searching over a predefined range (e.g., $k \in [0.5,2.0]$), we retain all k values for which the set of years satisfying $B < \mu - k \cdot \sigma$ exactly matches Y_{target}. The smallest and largest k in this valid range are denoted $k_{\min}$ and $k_{\max}$, respectively. These yield two thresholds:

$$\text{relaxed threshold} = \mu - k_{\min} \cdot \sigma, \ \text{strict threshold} = \mu - k_{\max} \cdot \sigma \quad (7)$$

The relaxed threshold serves as a lower bound for identifying potential extreme events, while the strict threshold denotes a more conservative bound for high-confidence extreme events. The interval between the two thresholds quantifies the uncertainty arising from the short training series.

Finally, for any year in the test set, we classify it as an extreme event if its mass balance falls below the relaxed threshold, and as a high-confidence extreme event if it falls below the strict threshold. To test the reliability and transferability of this dual-threshold framework, we validated it using five glaciers with long-term observational records across the TP, as presented in Sect. 5.2.

5. Results

5.1 Seasonal Cycle and Interannual Variation of Energy and Mass Balance

The seasonal variations in the glacier-wide energy balance and its components during the 2021/22 mass balance year are presented in Fig 4a. The S_{net} shows significant seasonal variability in the range of 30.2 W m^{-2} to 88.8 W m^{-2}, and this variability is mainly driven by the seasonal shift in the solar elevation angle in conjunction with the glacier surface albedo. L_{net} is the major energy-loss term for the glacier surface energy balance (Fig. 4a). The maximum and minimum values of net longwave radiation are -11.7 W m^{-2} and -87.5 W m^{-2}, which occur in August and March, respectively. The mean L_{net} in the warm and cool seasons are -33.2 W m^{-2} and -76.5 W m^{-2},

519 respectively. The difference in L_{net} between the warm and cool seasons mainly depends
520 on the difference between L_{in} and L_{out}. In this study, L_{in} is influenced by both air
521 temperature and relative humidity, both of which reach high values in the warm season,
522 corresponding to higher L_{in}. The L_{out} calculated from the glacier surface temperature
523 was also high during the warm season. Combining L_{in} and L_{out}, the absolute value of
524 L_{net} was found to be lower during the warm season than during the cold season. The Q_H
525 on Sangqu Glacier was continuously above 0 W m^{-2} and was an important heat source
526 in the energy balance (Fig. 4a). This indicates that the atmosphere continuously supplies
527 heat to the glacier surface, which helps maintain the glacier surface temperature. The
528 Q_H in the cold and warm seasons are 37 W m^{-2} and 49.4 W m^{-2}, respectively, and this
529 difference may be closely related to the temperature gradient between the glacier
530 surface and the atmosphere, as well as seasonal changes in wind speed. In contrast, the
531 Q_L on Sangqu Glacier is usually less than 0 W m^{-2}, and the mean Q_L is -21.8 W m^{-2},
532 indicating that sublimation or evaporation processes are continuously occurring at the
533 glacier surface (Fig. 4a). Q_G depends on the heat transfer coefficients of ice and snow,
534 as well as the temperature gradient (the temperature difference between the surface and
535 the interior of the glacier). The mean Q_G is 0.7 W m^{-2}, indicating that the Q_G accelerates
536 the melting process at the glacier surface (Fig. 4a). Further analysis showed that Q_G in
537 the cold season played an important role in maintaining the energy balance of the glacier
538 surface, whereas in the warm season, it accelerated the melting of the glacier surface.
539 Analysis of the combined energy components reveals that melt energy became positive
540 as early as March, marking the start of ablation on the Sangqu Glacier, with maximum
541 values occurring in July and August (Fig. 4a). This advanced melt onset corroborates
542 the observations of Zhu et al. (2024a). Additionally, melt energy decreases with
543 increasing elevation, reflecting the lower available energy at higher altitudes (Fig. S9).

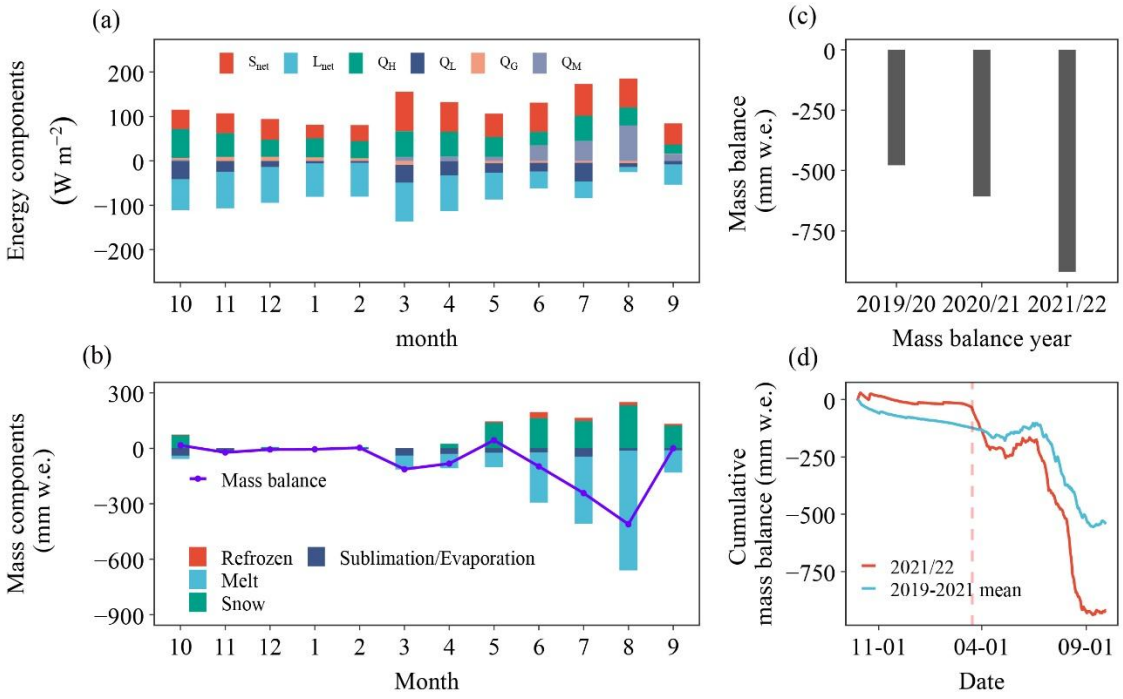


Figure 4. Monthly variations of (a) energy and (b) mass balance components during the 2021/22 mass balance year. (c) Interannual variations of annual mass balance. (d) Differences in accumulation mass balance between 2021/22 and the 2019–2021 mean.

The glacier-wide mass balance and its components at the glacial scale are shown in Fig. 4b. Melt, snowfall, refreezing, and sublimation/evaporation are the major mass components of glaciers on central TP.

Mass replenishment comes from snowfall and the refreezing of the snowpack. 73% of snowfall is concentrated in the warm season, and most precipitation falls as snow on glacier surfaces during the warm season. Cold–season snowfall accounts for only 27% of the total snowfall, with less mass replenishment. The total snowfall in April and May, which affects warm–season albedo and glacier melt rates, accounted for 18% of the total snowfall. Meltwater on the glacier surface and water content in the snow are the main sources of mass for refreezing. The volume of refreezing peaks in June, which is related to snow cover and meltwater on the glacier surface. During the observation period, the refreezing amount on Sangqu Glacier accounted for 6% of the melting amount.

The major mass losses from glaciers include melt, sublimation and evaporation.

The melt is the dominant component of the mass balance. Melting begins at the glacier surface in March and peaks in July or August, which is related to the seasonal distribution of melt energy. 85% of melt occurs during the warm season. June, July, August, and September account for 16%, 22%, 39%, and 7% of the total melt, respectively. Sublimation/evaporation is a component of the mass balance that cannot be ignored; in this study, sublimation/evaporation on the Sangqu Glacier accounted for 29% of the mass balance.

As illustrated in Fig 4c, the interannual variability in the mass balance of the Sangqu Glacier indicates that mass loss during the 2021/22 mass balance year was substantially more severe than in 2019/20 and 2020/21, surpassing those years by 442 mm w.e. and 312 mm w.e., respectively. Fig 4d shows the anomaly in cumulative mass balance for 2021/22 relative to the 2019–2021 average. This further indicates that the cumulative mass balance in 2021/22 began to diverge negatively from the multi-year average earlier in the year, suggesting an earlier onset of rapid ablation compared to the two preceding mass balance years.

5.2 Identification and Validation of Extreme Glacier Mass Loss Events on TP

To evaluate the robustness of our proposed dual-threshold framework across different climatic regimes and record lengths, we applied it to five glaciers with long-term mass balance observations on the TP (Fig 1a, Fig. 5, and Fig. S4). These five glaciers were selected to represent the major climatic regimes of the Tibetan Plateau: Xiao Dongkemadi Glacier in the central plateau (relatively humid, summer-accumulation type), Qiyi Glacier and Ningchan No. 1 Glacier in the northern Qilian Mountains (arid continental), and Guliya Glacier and Xiao Anglong Glacier in the western Kunlun Mountains (hyper-arid, cold). This broad spatial coverage allows us to evaluate the transferability and robustness of our dual-threshold framework under diverse climatic and glaciological conditions, thereby strengthening the credibility of its application to the short-term record of Sangqu Glacier.

Following the methodology described in Sect. 4.4, we first calibrated the multiplier k for each glacier based on the training period. The resulting k_{min} and k_{max} values vary by glacier: for Xiao Dongkemadi Glacier, k_{min} of 1.06 and k_{max} of 1.13; for Qiyi Glacier,

592 k_{min} of 1.28 and k_{max} of 1.34; and for Guliya Glacier, k_{min} of 1.29 and k_{max} of 1.34 (Fig.
593 5). For Ningchan No. 1 Glacier and Xiao Anglong Glacier, the corresponding values
594 are presented in Fig. S4. Using these k values, the relaxed and strict thresholds (as
595 defined in Sect. 4.4) were calculated, enabling the identification of 4–6 extreme mass
596 loss events across the five glaciers. This demonstrates that the framework reliably
597 identifies extreme events even when applied to short-term records.

598 Given the climatic similarity between Xiao Dongkemadi Glacier and Sangqu
599 Glacier, we applied the k values derived from the former to assess the severity of the
600 2021/22 mass balance year at Sangqu Glacier. Using the mean and standard deviation
601 of the 2019–2021 mass balance record at Sangqu Glacier, the relaxed and strict
602 thresholds were calculated as –925.1 mm w.e. and –909.2 mm w.e., respectively. The
603 simulated annual mass balance for 2021/22 (–919.8 mm w.e.) falls between these two
604 thresholds, confirming that this mass balance year qualifies as an extreme mass loss
605 event.

606 This finding is further substantiated by two independent datasets (Hugonnet et al.,
607 2021; Dussaillant et al., 2025). First, satellite-derived glacier mass balance estimates
608 (2000–2019) indicate that the 2021/22 mass loss was approximately twice the annual
609 average for the period 2000–2019 (Fig. S5). Second, global 0.5°-resolution glacier mass
610 balance data (1976–2022) show that the 2021/22 values were 600–700 mm w.e. lower
611 than the 1976–2021 mean (Fig. S6). Collectively, these multi-source datasets provide
612 compelling evidence that the 2021/22 mass loss at Sangqu Glacier was unprecedented
613 in recent decades.

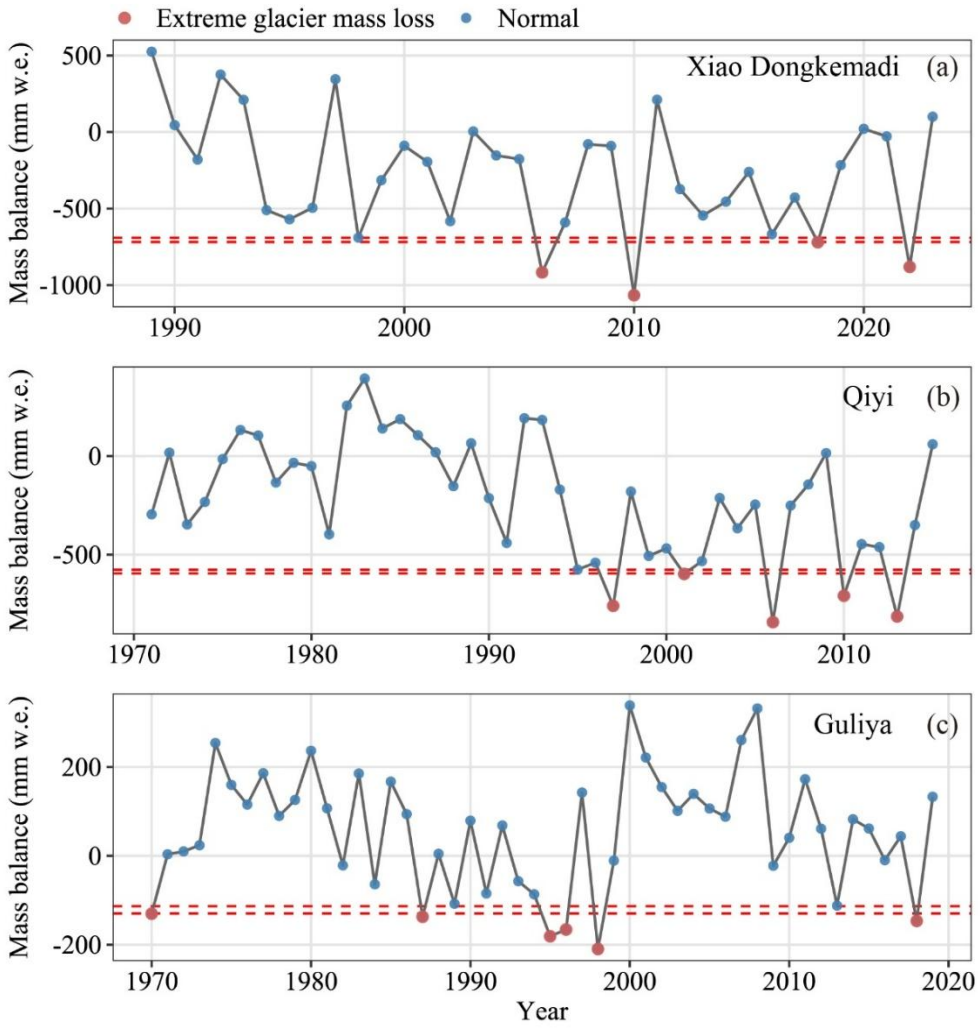


Figure 5. Annual mass balance time series and extreme mass loss events for (a) Xiao Dongkemadi Glacier, (b) Qiyi Glacier, and (c) Guliya Glacier. The data were sourced from Yao et al. (2012), Zhu et al. (2026a) and Zhu et al. (2022a, 2022b). The red dashed line indicates the threshold for identifying extreme mass loss events.

5.3 Surface Energy Balance Responsible for Extreme Melt during summer 2022 heatwave

We conducted a rigorous analysis of the glacier-wide energy balance on Sangqu Glacier during the 2022 summer heatwave, which induced extreme melt. Our results reveal distinct energy balance anomalies associated with this event, as illustrated in Figs 6 and S7.

Relative to the reference period (October 2019–September 2021), the extreme melt period was characterized by a 2.9 W m^{-2} decrease in S_{in} (Fig. 6a) and an 8.0 W m^{-2}

reduction in S_{out} (Fig. S7a). The decline in S_{out} was primarily driven by a 3.5% decrease in albedo (Fig. 6b), resulting in a S_{net} gain of 5.1 W m^{-2} (Fig. S7e). Longwave radiation components also exhibited substantial changes: L_{in} increased by 20.3 W m^{-2} (Fig. 6c), while L_{out} rose by 6.3 W m^{-2} (Fig. S7b). This led to a L_{net} increase of 14.0 W m^{-2} (Fig. S7f). Combined, the increases in S_{net} and L_{net} contributed an additional 19.1 W m^{-2} to the total net radiation.

Regarding turbulent heat fluxes, Q_H showed a marked increase of 17.0 W m^{-2} (Fig. 6d), whereas Q_L decreased by 4.8 W m^{-2} (Fig. S7c). Q_G also declined by 5.0 W m^{-2} (Fig. S7d). These energy balance anomalies substantially enhanced the energy available for melt (Fig. 6e), driven by increased L_{in} and Q_H, alongside reductions in S_{out}, Q_L, and Q_G. The amplified S_{net} resulting from reduced albedo, combined with enhanced L_{in} and Q_H due to warm air advection, ultimately led to the extreme melt during the heatwave. Under these energy balance anomalies, the average melt energy during the heatwave from June to September 2022 increased by 30.7 W m^{-2}, resulting in an exceptional rise in melt amount of 317.8 mm w.e.. The melt amount during this period was 1.66 and 1.69 times that recorded for the same period in 2020 and 2021, respectively.

Current research increasingly identifies energy balance anomalies as the principal driver of extreme glacier melt. Zhu et al. (2024a) demonstrated that early 2022 springtime climatic extremes interacting with anomalous S_{in} and Q_H triggered exceptional melting on Sangqu Glacier. Thibert et al. (2018) reported record melt on Sarennes Glacier (French Alps) controlled by three factors: S_{in} anomalies, Q_L variations, and preseason snowpack conditions. Tian et al. (2023) further established that large-scale circulation patterns modulating cloud cover diurnal cycles induced extreme temperature anomalies in the eastern TP.

Our findings corroborate that energy balance anomalies, characterized by L_{in} enhancement, Q_H amplification, and albedo reduction, were the primary drivers of glacier melt during the 2022 summer heatwave. The observed energy partitioning pattern, featuring synergistic radiative-turbulent flux interactions during these summer extreme events, aligns with documented mechanisms in both Alpine and TP glaciers (Thibert et al., 2018; Zhu et al., 2024a).

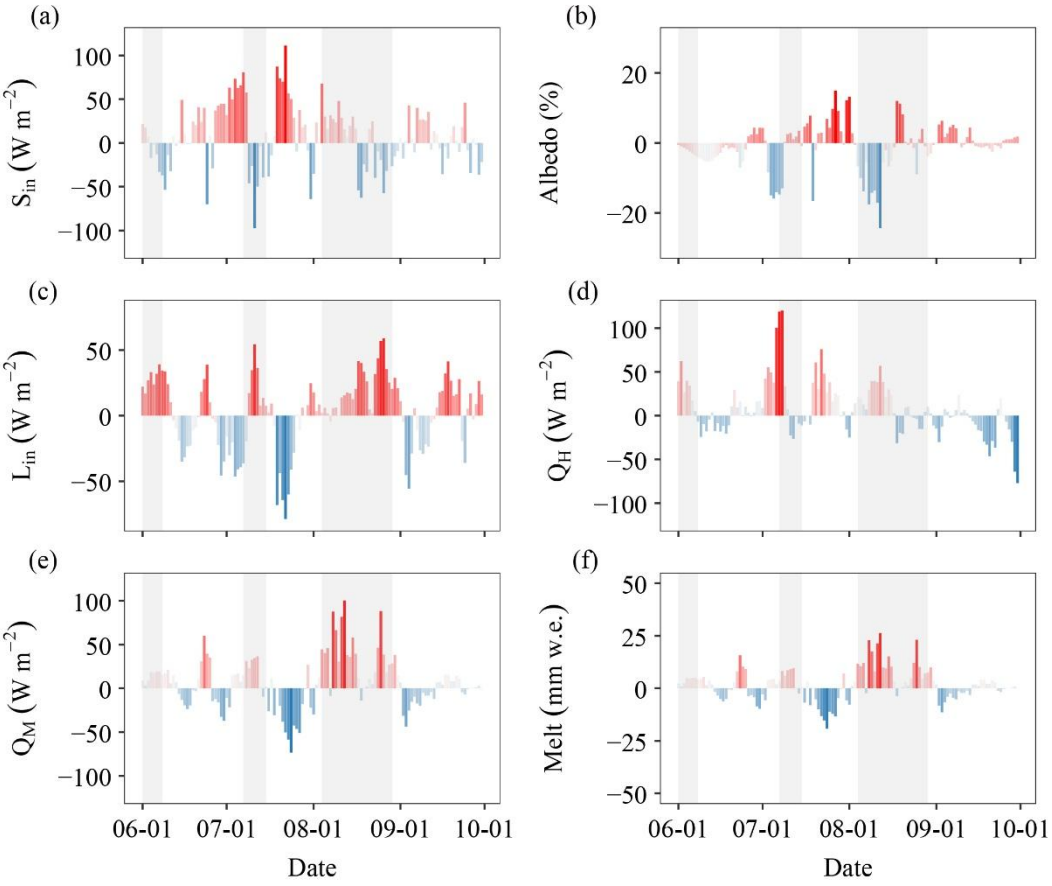


Figure 6. Glacier-wide energy balance anomalies associated with the extreme melt events. Anomalies in (a) incoming shortwave radiation, (b) albedo, (c) incoming longwave radiation, (d) sensible heat flux, (e) melt energy, and (f) melt amount are shown relative to the reference period October 2019–September 2021. Gray shading indicates the 2022 summer heatwave period (June–September).

6. Discussion

6.1 Effects of Atmospheric Circulation on Extreme Glacier Melt and heat waves

A growing body of research indicates that large-scale circulation anomalies influence glacier mass balance over the TP and its surrounding regions by modulating temperature and precipitation patterns (Yao et al., 2012). Specific configurations of these anomalies, particularly those leading to extreme high-temperature events, have had marked impacts on glacier mass balance in the region. Previous studies have identified the Western Pacific subtropical high, the South Asian high, and the westerly circulation as the primary large-scale systems affecting the plateau. This study finds that during the 2022 summer heatwave, the Western Pacific subtropical high exhibited

673 a pronounced westward extension relative to its climatological mean (Fig. 7b), while
674 the South Asian high extended anomalously eastward (Fig. 7a). Additionally, the
675 meridional displacement of the westerly jet stream played a crucial role, as captured by
676 the subtropical westerly jet (SWJ index) defined as the first principal component of an
677 empirical orthogonal function (EOF) analysis of 200 hPa zonal winds over the region
678 20°N–50°N, 40°E–90°E (Wei and Yu, 2024). The spatial pattern of the first EOF mode
679 shows positive anomalies between 40°N and 50°N and negative anomalies between
680 25°N and 35°N, indicating a northward shift of the westerly circulation during the 2022
681 summer heatwave (Fig. 7c). Time series analysis further supports this northward
682 displacement, with the SWJ index exhibiting a sustained positive phase over the same
683 period (Fig. 7d).

684 Subsequent studies have reinforced the role of anomalies in the Western Pacific
685 subtropical high, South Asian high, and westerly circulation in driving extreme high
686 temperatures over the TP. Zhou et al. (2024) found that in the summer of 2022, the
687 Western Pacific subtropical high extended anomalously westward, while the Iranian
688 high extended northeastward. Concurrently, an expanded influence of the South Asian
689 high subjected the plateau to a barotropic high-pressure system. This circulation
690 configuration, accompanied by a northward shift of the subtropical westerly jet, reduced
691 moisture transport toward the TP (Wang et al., 2017).

692 These large-scale circulation anomalies also produced significant local effects.
693 During the summer heatwave, increased cloud cover (Fig. S10b) and a substantial rise
694 in downward longwave radiation (Fig. S10c) contributed to elevated air temperatures
695 (Fig. S10a). This warming was accompanied by increased soil temperatures (Fig. S10e)
696 and decreased soil moisture due to enhanced evaporation (Fig. S10f). The resulting dry
697 soil conditions are not merely a passive response to atmospheric forcing but can
698 feedback onto the circulation system. Jiang et al. (2024) suggest that soil drought over
699 the TP can further sustain and even intensify the northward shift of the subtropical
700 westerly jet by exciting quasi-stationary Rossby waves. Furthermore, the drier surface
701 enhances the upward sensible heat flux (Fig. S10d), which warms the mid-to-upper

troposphere, providing favorable local thermodynamic conditions for the maintenance of the barotropic high-pressure system and the persistence of the heatwave.

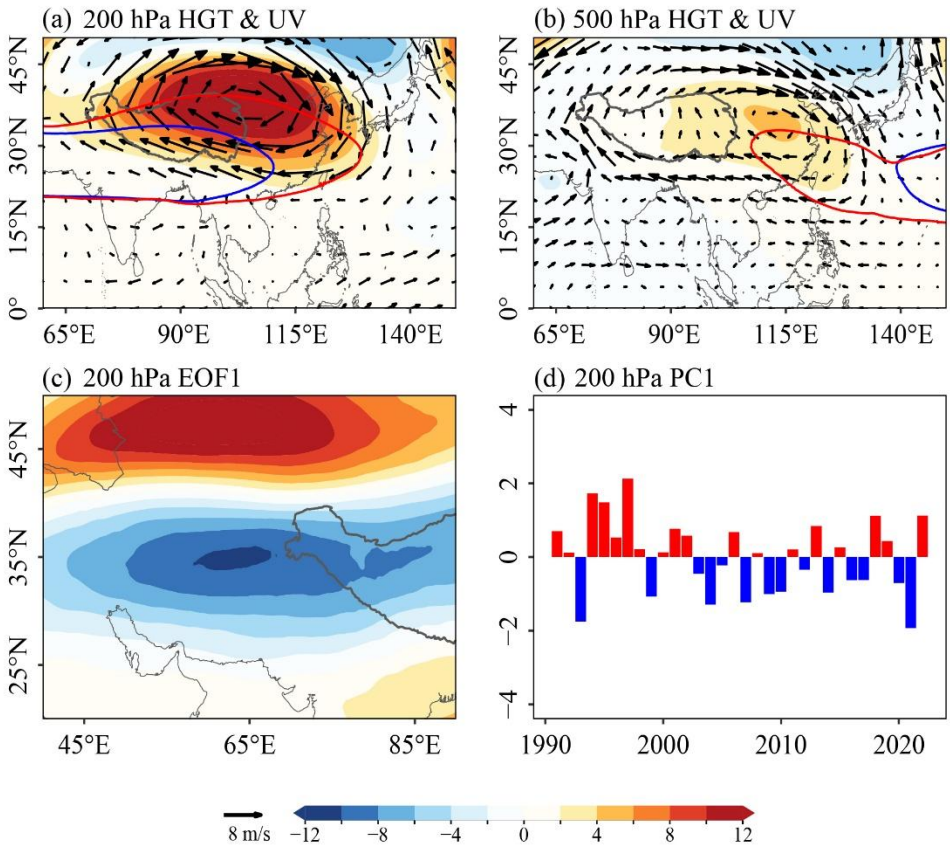


Figure 7. Atmospheric circulation anomalies and dominant modes during the 2022 summer heatwave. Anomalies are calculated relative to the 1992–2021 climatology. (a, b) Spatial distribution of geopotential height (shading) and horizontal wind (vectors) at (a) 200 hPa and (b) 500 hPa during the 2022 summer heatwave. (c) The first leading EOF mode of 200 hPa zonal wind anomalies averaged over the same calendar periods as the 2022 heatwave (1–8 June, 7–15 July, and 4–29 August) for each year from 1991 to 2022, over the region (20°–50°N, 40°–90°E). (d) The corresponding normalized principal component (PC1) time series for 1991–2022. The blue solid (dashed) contour in (a) represents the 1250 gpm isopleth at 200 hPa. The blue solid (dashed) contour in (b) represents the 5880 gpm isopleth at 500 hPa.

6.2 Comparison with extreme glacier mass loss events in other regions

In recent years, investigations conducted in diverse mountain glacier regions across the globe have examined extreme mass loss events. These regions include Switzerland (Cremona et al., 2023; Van Tiel et al., 2026), Austria (Voordendag et al., 2023), the Arctic Svalbard (Bernard and Friedt, 2025), the Pyrenees (Izagirre et al., 2024), the Tien Shan in China (Xu et al., 2024), western Canada and the United States

720 (Menounos et al., 2025), the central TP (Zhu et al., 2024a), and New Zealand (Vargo et
721 al., 2020). These studies have revealed common characteristics and driving mechanisms
722 underlying such events. The distinctive features include record ablation rates and rapid
723 glacier state degradation. In the Swiss Alps, glacier mass loss in 2022 was more than
724 triple the 1991–2020 average, with summer melt intensity breaking observational
725 records. In basins with 15% glacier cover, this summer ice melt compensated for
726 precipitation and snowmelt deficits (Van Tiel et al., 2026). In the Pyrenees, glacier area
727 shrank by nearly 40% between 2020 and 2023, with thinning rates more than three
728 times those of the previous decade (Izagirre et al., 2024). Urumqi Glacier No. 1 in the
729 Tien Shan also recorded severe mass loss in 2022 (Xu et al., 2024). Glaciers on the
730 central TP experienced anomalous melting in early spring, a season typically considered
731 part of the accumulation period (Zhu et al., 2024a). In western Canada and the United
732 States, mass loss rates between 2021 and 2024 doubled relative to 2010–2020,
733 cumulatively reducing glacier mass by 12% (Menounos et al., 2025).

734 The mechanisms driving these extreme mass loss events involve multiple
735 interacting factors. First, anomalous large-scale atmospheric circulation provided the
736 background conditions for extreme weather and climate events. The weakening and
737 northward shift of the mid-latitude westerly jet stream, for instance, disrupted cold
738 moist air transport to the TP, leading to persistent high temperatures (Zhu et al., 2024a).
739 Second, record-breaking summer heatwaves superimposed on deficient winter snowfall
740 directly supplied substantial energy for glacier melt (Menounos et al., 2025; Xu et al.,
741 2024). From an energy balance perspective, this anomaly manifested as significant
742 increases in incoming shortwave radiation due to reduced cloud cover and in sensible
743 heat flux. On Sarennes Glacier in the French Alps, for example, the extreme melt in
744 2003 was dominated by a substantial increase in global radiation and sensible heat flux
745 (Thibert et al., 2018). Finally, a key accelerating mechanism is the albedo feedback on
746 glacier surfaces: high temperatures lead to earlier snowmelt, exposing lower-albedo ice.
747 The deposition of black carbon from wildfires in North America or Saharan dust in the
748 Alps further reduces albedo, causing the glacier to absorb more solar radiation and
749 thereby establishing a feedback loop that amplifies melting (Menounos et al., 2025; Van

Tiel et al., 2026). Event attribution studies in New Zealand have confirmed that anthropogenic warming made extreme mass loss years like 2011 and 2018 at least six to ten times more likely (Vargo et al., 2020). Research on Austre Lovénbreen in the Arctic revealed that a heatwave and liquid precipitation event in March 2022 altered snowpack structure, significantly advancing glacier ice exposure and prolonging the melt season. This represents another crucial mechanism exacerbating mass loss (Bernard and Friedt, 2025). In the same year at Hintereisferner in Austria, extremely low winter accumulation, 43% below the 2011–2020 average, combined with an early melt season onset to advance the Glacier Loss Day to 23 June, 49 days earlier than normal. This ultimately resulted in annual mass loss 3.2 times the 1991–2020 average (Voordendag et al., 2023). These extreme glacier mass loss events are driven by a combination of interacting mechanisms. Anomalous atmospheric circulation patterns and record-breaking heatwaves provide the energy background, while winter snow deficits, snowpack destabilization induced by liquid precipitation, and albedo feedback collectively lead to earlier glacier ice exposure and a prolonged melt season, thereby synergistically intensifying glacier ablation.

Therefore, glaciers across global mountain regions exhibited common characteristics of extreme mass loss, including record-breaking ablation rates, accelerated area shrinkage and thinning, and a short-term hydrological buffering effect that compensated for precipitation deficits. These extreme melt events were driven synergistically by anomalous large-scale atmospheric circulation and record summer heatwaves, amplified by mechanisms such as winter snow deficits, liquid precipitation-induced snowpack destabilization, and surface albedo feedback, underscoring the need for systematic research on more frequent extreme events.

6.3 Implications of Extreme Heatwaves and Glacier Melt Events for Hydrological Processes

In glacier-fed basins, extreme weather and climate events, such as extreme heat, drought, and heavy precipitation, strongly influence glacier melt and hydrological processes. Research across the Arctic (Boon et al., 2003), Greenland (Kondo et al., 2021), the Canadian Rockies (Anderson and Radić, 2023), the European Alps

(Koboltschnig et al., 2009; Koboltschnig and Schöner, 2011; Van Tiel et al., 2026), and the TP (Zhu et al., 2024b) shows that extreme heat-driven melt events affect basin runoff across three timescales: short-term hazards, seasonal water allocation, and long-term trends.

On short timescales, extreme heat intensifies turbulent heat fluxes and triggers albedo feedback, causing melt rates and runoff to surge within days. Studies from the High Arctic (Boon et al., 2003), Greenland (Kondo et al., 2021), and the European Alps (Koboltschnig et al., 2009) document that such events can produce large fractions of seasonal ablation in just a few days or generate flash floods when combined with strong winds.

At the seasonal scale, extreme melt events alter the timing and composition of runoff. Spring heatwaves often cause early snow depletion, leading to runoff deficits later in the season. In glacierized basins, sustained summer melt can partially offset these deficits, whereas non-glacierized basins experience sharp declines (Anderson and Radić, 2023). Evidence from Austria and the TP further shows that during extreme heatwaves (Koboltschnig and Schöner, 2011; Zhu et al., 2024b), glacier melt contributions can increase even when total runoff drops, a pattern linked to albedo feedback, which consistently amplifies melt across different climatic regions.

Over the long term, however, this buffering capacity is weakening. Despite record-high summer temperatures and melt rates, total meltwater volumes have declined in recent extreme years due to glacier area loss, indicating that continued glacier shrinkage can offset the effect of even extreme heat (Van Tiel et al., 2026).

Taken together, these findings highlight that the response of glacierized basins to extreme heat is shaped by thermal forcing, glacier characteristics (such as snowline, bare ice extent, and ice volume), and long-term climate change. Current evidence suggests a shift from a linear melt response to a nonlinear phase, characterized by rising short-term flood risks, declining long-term water supply, and fundamental changes in runoff composition.

808 **6.4 Research Limitations**

809 While this study integrates multi-source data with an energy-mass balance model
810 to reveal the extreme melting processes and mechanisms of the Sangqu Glacier on the
811 central TP driven by the 2022 summer heatwave, several limitations warrant further
812 investigation.

813 The AWS was deployed at only a single elevation point on the glacier surface,
814 resulting in spatiotemporal gaps that make spatial extrapolation of meteorological
815 variables a primary source of model uncertainty. We used parameterization schemes
816 such as temperature lapse rates and precipitation gradients to extrapolate point-scale
817 observations to the entire glacier and conducted sensitivity analyses. However, this
818 simplified approach cannot fully capture the spatiotemporal heterogeneity of
819 meteorological variables under complex terrain conditions, which may introduce
820 uncertainty especially during extreme weather and climate events. Other studies have
821 also indicated that even with physically robust energy balance models, spatial
822 extrapolation of meteorological variables remains a major source of model uncertainty
823 requiring multi-source data constraints (Kinnard et al., 2022). Moreover, logistical
824 challenges on the TP, such as power failures and harsh environmental conditions,
825 persistently hamper field data continuity. We used observational data as much as
826 possible to constrain the model and employed mass balance observations from the
827 adjacent Xiao Dongkemadi Glacier (2021/22) for independent validation, yet these data
828 gaps inevitably affect the precision of interannual comparisons.

829 We did not apply explicit seasonal bias correction to the downscaled ERA5 data.
830 However, validation for the ablation season (Fig. S8) shows good agreement with
831 observations, suggesting minimal seasonal bias during summer. Nevertheless, this
832 simplification may introduce uncertainties under extreme conditions and should be
833 addressed in future work. Additionally, while we used a random forest method to
834 statistically downscale ERA5 reanalysis data, the inherent errors of the downscaling
835 model were not incorporated into the final uncertainty assessment, a factor that could
836 be significant under extreme climatic anomalies.

837 While the EBFM performs well at the glacier-wide scale, discrepancies are evident

838 at finer scales (point and seasonal), reflecting inherent challenges of distributed glacier
839 modeling under data-scarce conditions. These deviations arise from spatial
840 extrapolation of meteorological variables using simplified lapse rates and gradients,
841 parameterization uncertainty (with albedo and temperature lapse rate being the most
842 sensitive parameters), scale mismatch between point stakes and grid-cell averages, and
843 observational uncertainties in density assumptions and stake height readings. Despite
844 these limitations, the model's accuracy at the glacier-wide scale is sufficient for our
845 extreme event analysis, and independent verification from the neighboring Xiao
846 Dongkemadi Glacier supports the reliability of our conclusions.

847 The EBFM employed in this study has been validated at multiple scales, but its
848 calibration of key parameters, including snow/ice albedo, turbulent exchange
849 coefficients, and precipitation gradients, relies on limited observational data. This
850 introduces uncertainties in the key parameterization schemes and may affect the model's
851 extrapolation capability under extreme conditions. Studies in other regions have shown
852 that different combinations of parameterization schemes can lead to considerable
853 differences in the simulated individual energy flux components while having a
854 relatively smaller impact on total melting energy, suggesting that total melt is less
855 sensitive to different parameterization schemes than the individual flux components
856 themselves (Draeger et al., 2024). This finding is consistent with the results of our
857 sensitivity analysis. Nevertheless, our uncertainty assessment through parameter
858 perturbation may still not fully capture the nonlinearities inherent in heatwave-driven
859 processes. Additionally, the model does not account for snow redistribution processes
860 such as wind-driven transport and avalanches, which may influence the spatial
861 distribution of mass balance, particularly in complex terrain.

862 A simplification in this study is the assumption of fixed glacier geometry, which
863 neglects the feedback effects of glacier thinning and area retreat on mass balance. This
864 feedback is inherently nonlinear: surface elevation lowering leads to higher air
865 temperatures, while glacier terminus retreat can alter local precipitation patterns.
866 Particularly during extreme melt years, rapid changes in glacier geometry can modify
867 the local energy budget, and neglecting this process may bias melt magnitude estimates.

For instance, Bolibar et al. (2022) demonstrated that topographic feedback resulting from glacier retreat to higher elevations can partially compensate for the negative impacts of climatic warming on mass balance, whereas a fixed-geometry assumption tends to overestimate melt sensitivity. More critically, the fixed-geometry assumption limits our understanding of the evolution of total glacier melt. As shown by Van Tiel et al. (2026) in the Swiss Alps, the reduction in glacier area can eventually supersede enhanced melt rates as the dominant driver of total discharge. Therefore, future research should couple energy-balance models with ice dynamics and incorporate multi-temporal glacier boundary data to better resolve the transient response of glacier mass balance to extreme climate conditions and its downstream hydrological impacts.

This study focused on Sangqu Glacier on the central TP, which is situated at the confluence of the mid-latitude westerlies and the Indian monsoon. Consequently, the regional generalizability of our findings requires broader validation. Glacier sensitivity to climatic anomalies varies markedly across the TP, from the humid southeast to the arid northwest (Yao et al., 2012; Zhu et al., 2018). Whether the extreme melting mechanism identified here, driven by enhanced sensible heat flux, increased downward longwave radiation, and reduced albedo, can be directly extended to other glacier types remains to be examined through similar studies in more representative sub-regions. Future research should strengthen multi-glacier collaborative observation networks and integrate high-resolution regional climate modeling to deepen our understanding of extreme melt mechanisms across diverse climatic regimes.

7. Conclusion

This study integrated in situ glacio-meteorological observations from Sangqu Glacier with a surface energy–mass balance model to elucidate the mechanisms driving extreme glacier melt during the 2022 summer heatwave. To overcome the challenge of identifying extreme mass loss from short-term records, we developed a dual-threshold framework based on the mean and standard deviation. This approach effectively identifies extreme events in data-scarce regions, providing a robust diagnostic tool that circumvents the traditional requirement for decadal observational series.

Our findings reveal that the 2021/22 mass balance year experienced unprecedented

mass loss. During the 2022 summer heatwave, glacier melt was 1.66 and 1.69 times higher than in the corresponding periods of 2019/20 and 2020/21, respectively, corresponding to an increase of 317.8 mm w.e.. This intensified melting was driven by synergistic anomalies in the surface energy balance, namely reduced albedo, enhanced downward longwave radiation, and increased sensible heat flux. These local-scale drivers were modulated by large-scale atmospheric circulation patterns, characterized by the westward expansion and intensification of the Western Pacific Subtropical High, the eastward extension of the South Asian High, and the poleward shift of the westerlies.

In summary, this study improves our understanding of glacier mass balance responses to extreme weather and climate events on the central TP. The findings highlight the critical role of glacier surface energy balance anomalies in driving extreme melt during heatwaves and emphasize the importance of large-scale atmospheric circulation anomalies. This study has certain limitations, mainly including the limited spatial representativeness due to single-point meteorological observations and the omission of feedback effects from dynamic glacier geometry changes on mass balance. Future research should conduct detailed in situ observations of glacier surface micrometeorology, mass balance, and runoff across different climatic zones on the TP to further elucidate the mechanisms of extreme melt during summer heatwaves and their impacts on hydrological processes, thereby providing a scientific basis for water resource management and hazard risk assessment.

Acknowledgements We thank the editor and anonymous reviewers for their constructive feedback on the manuscript, which led to substantial improvements during the review process.

Code and Data Availability Statement Meteorological data from the Tuotuohe meteorological station was obtained from the China Meteorological Administration's website (http://data.cma.cn/). ERA5 is available for download at https://cds.climate.copernicus.eu/cdsapp#!/search?type=dataset. The EBFM model is available via https://github.com/wardvp/EBFM - glacier. The Dual-Threshold Framework can be found at https://github.com/zhuzhufeifei/detect_extreme_events. Data supporting the

findings of this study are available from the corresponding author upon reasonable request.

Author contribution All authors contributed to the study conception and design. Data collection was performed by F. Z. Analysis was performed by F. Z, M. Z and L. A. The first draft of the manuscript was written by F. Z and all authors commented on previous versions of the manuscript. All authors read and approved of the final manuscript.

Competing interests: The authors declare that they have no conflict of interest.

Financial support This study is jointly funded by the Second Tibetan Plateau Scientific Expedition and Research Program (2024QZKK0400 and 2024QZKK0100) and the Science and Technology Project of the Xizang Autonomous Region (XZ202501ZY0081 and XZ202501JD0025).

References

Anderson, S. and Radic, V.: Modeling the Streamflow Response to Heatwaves Across Glacierized Basins in Southwestern Canada, Water Resour. Res., 59, https://doi.org/10.1029/2023WR035428, 2023.

Bernard, É. and Friedt, J.-M.: Did a global heatwave have a lasting impact on the snowpack and the annual glacier mass balance? The example of a small glacial basin observatory in the High Arctic (Brøgger Peninsula, Spitsbergen), Arctic, Antarctic, and Alpine Research, 57, 2479899, https://doi.org/10.1080/15230430.2025.2479899, 2025.

Bhattacharya, A., Bolch, T., Mukherjee, K., King, O., Menounos, B., Kapitsa, V., Neckel, N., Yang, W., and Yao, T.: High Mountain Asian glacier response to climate revealed by multi-temporal satellite observations since the 1960s, Nat. Commun., 12, 4133, https://doi.org/10.1038/s41467-021-24180-y, 2021.

Bolch, T., Kulkarni, A., Kääb, A., Huggel, C., Paul, F., Cogley, J. G., Frey, H., Kargel, J. S., Fujita, K., Scheel, M., Bajracharya, S., and Stoffel, M.: The State and Fate of Himalayan Glaciers, Science, 336, 310–314, https://doi.org/10.1126/science.1215828, 2012.

Bolibar, J., Rabatel, A., Gouttevin, I., Zekollari, H., and Galiez, C.: Nonlinear sensitivity of glacier mass balance to future climate change unveiled by deep learning, Nat. Commun., 13, 409, https://doi.org/10.1038/s41467-022-28033-0, 2022.

Bougamont, M., Bamber, J. L., and Greuell, W.: A surface mass balance model for the Greenland Ice Sheet, J. Geophys. Res.: Earth Surf., 110, https://doi.org/10.1029/2005JF000348, 2005.

Boon, S., Sharp, M., and Nienow, P.: Impact of an extreme melt event on the runoff and hydrology of a high Arctic glacier, Hydrol. Processes, 17, 1051–1072, https://doi.org/10.1002/hyp.1194, 2003.

Brun, F., Berthier, E., Wagnon, P., Kääb, A., and Treichler, D.: A spatially resolved estimate of High Mountain Asia glacier mass balances from 2000 to 2016, Nat. Geosci., 10, 668–673, https://doi.org/10.1038/ngeo2999, 2017.

Brunt, D.: Notes on radiation in the atmosphere. I, Q. J. R. Meteorolog. Soc., 58, 389–420, https://doi.org/10.1002/qj.49705824704, 1932.

Chen, J., Xue, X., and Du, W.: Short communication: Extreme glacier mass loss triggered by high temperature and drought during hydrological year 2022 / 2023 in Qilian Mountains, Res. Cold Arid Reg., 16, 1–4, https://doi.org/10.1016/j.rcar.2024.01.002, 2024.

Cremona, A., Huss, M., Landmann, J. M., Borner, J., and Farinotti, D.: European heat waves 2022: contribution to extreme glacier melt in Switzerland inferred from automated ablation readings, Cryosphere, 17, 1895–1912, https://doi.org/10.5194/tc-17-1895-2023, 2023.

Draeger, C., Radić, V., White, R. H., and Tessema, M. A.: Evaluation of reanalysis data and dynamical downscaling for surface energy balance modeling at mountain glaciers in western Canada, Cryosphere, 18, 17–42, https://doi.org/10.5194/tc-18-17-2024, 2024.

Duan, J., Zhang, H., Jian, D., Xiao, C., Hao, F., Zhu, H., Lott, F. C., and Stott, P. A.: Influences of Anthropogenic Forcing on the Exceptionally Warm August 2022 over the Eastern Tibetan Plateau, Bull. Am. Meteorol. Soc., 105, E1068–E1073, https://doi.org/10.1175/BAMS-D-23-0179.1, 2024.

Duan, Q., Sorooshian, S., and Gupta, V.: Effective and efficient global optimization for conceptual rainfall-runoff models, Water Resour. Res., 28, 1015–1031, https://doi.org/10.1029/91WR02985, 1992.

Dussaillant, I., Hugonnet, R., Huss, M., Berthier, E., Bannwart, J., Paul, F., and Zemp, M.: Annual mass change of the world's glaciers from 1976 to 2024 by temporal downscaling of satellite data with in situ observations, Earth Syst. Sci. Data, 17, 1977–2006, https://doi.org/10.5194/essd-17-1977-2025, 2025.

Fujita, K., Seko, K., Ageta, Y., Jianchen, P., and Tandong, Y.: Superimposed ice in glacier mass balance on the Tibetan Plateau, J. Glaciol., 42, 454–460, https://doi.org/10.3189/S0022143000003440, 1996.

Gao, H., He, X., Ye, B., and Pu, J.: Modeling the runoff and glacier mass balance in a small watershed on the Central Tibetan Plateau, China, from 1955 to 2008, Hydrol. Processes, 26, 1593–1603, https://doi.org/10.1002/hyp.8256, 2012.

Guo, W., Liu, S., Xu, J., Wu, L., Shangguan, D., Yao, X., Wei, J., Bao, W., Yu, P., Liu, Q., and Jiang, Z.: The second Chinese glacier inventory: data, methods and results, J. Glaciol., 61, 357–372, https://doi.org/10.3189/2015JoG14J209, 2015.

Hock, R. and Holmgren, B.: A distributed surface energy-balance model for complex topography and its application to Storglaciären, Sweden, J. Glaciol., 51, 25–36, https://doi.org/10.3189/172756505781829566, 2005.

Hoffmann, L., Günther, G., Li, D., Stein, O., Wu, X., Griessbach, S., Heng, Y., Konopka, P., Müller, R., Vogel, B., and Wright, J. S.: From ERA-Interim to ERA5: the considerable impact of ECMWF's next-generation reanalysis on Lagrangian transport simulations, Atmos. Chem. Phys., 19, 3097–3124, https://doi.org/10.5194/acp-19-3097-2019, 2019.

Hua, W., Dai, A., Qin, M., Hu, Y., and Cui, Y.: How Unexpected Was the 2022 Summertime Heat Extremes in the Middle Reaches of the Yangtze River?, Geophys. Res. Lett., 50, e2023GL104269, https://doi.org/10.1029/2023GL104269, 2023.

Hugonnet, R., McNabb, R., Berthier, E., Menounos, B., Nuth, C., Girod, L., Farinotti, D., Huss, M., Dussaillant, I., Brun, F., and Kääb, A.: Accelerated global glacier mass loss in the early

twenty-first century, Nature, 592, 726–731, https://doi.org/10.1038/s41586-021-03436-z, 2021.

Izagirre, E., Revuelto, J., Vidaller, I., Deschamps-Berger, C., Rojas-Heredia, F., Rico, I., Alonso-González, E., Gascoin, S., Serrano, E., and López-Moreno, J. I.: Pyrenean glaciers are disappearing fast: state of the glaciers after the extreme mass losses in 2022 and 2023, Reg Environ Change, 24, 172, https://doi.org/10.1007/s10113-024-02333-1, 2024.

Jeong, H., Park, H.-S., Chowdary, J. S., and Xie, S.-P.: Triple-Dip La Niña Contributes to Pakistan Flooding and Southern China Drought in Summer 2022, Bull. Am. Meteorol. Soc., 104, E1570–E1586, https://doi.org/10.1175/BAMS-D-23-0002.1, 2023.

Jiang, J., Liu, Y., Meng, J., Wu, G., He, B., Ma, T., Bao, W., and Fan, J.: Dry soil moisture on the Tibetan Plateau drives synchronous extreme heatwaves in Europe and east Asia, npj Clim. Atmos. Sci., 7, 281–290, https://doi.org/10.1038/s41612-024-00831-x, 2024.

K. Deb, A. Pratap, S. Agarwal, and T. Meyarivan: A fast and elitist multiobjective genetic algorithm: NSGA-II, IEEE Trans. Evol. Comput., 6, 182–197, https://doi.org/10.1109/4235.996017, 2002.

Kang, S., Wang, F., Morgenstern, U., Zhang, Y., Grigholm, B., Kaspari, S., Schwikowski, M., Ren, J., Yao, T., Qin, D., and Mayewski, P. A.: Dramatic loss of glacier accumulation area on the Tibetan Plateau revealed by ice core tritium and mercury records, Cryosphere, 9, 1213–1222, https://doi.org/10.5194/tc-9-1213-2015, 2015.

King, O., Ghuffar, S., Bhattacharya, A., Yao, R., Yao, T., and Bolch, T.: Glaciological and climatological drivers of heterogeneous glacier mass loss in the Tanggula Shan (Central-Eastern Tibetan Plateau), since the 1960s, J. Glaciol., 69, 1149–1166, https://doi.org/10.1017/jog.2023.5, 2023.

Kinnard, C., Larouche, O., Demuth, M. N., and Menounos, B.: Modelling glacier mass balance and climate sensitivity in the context of sparse observations: application to Saskatchewan Glacier, western Canada, Cryosphere, 16, 3071–3099, https://doi.org/10.5194/tc-16-3071-2022, 2022.

Koboltschnig, G. R., Schöner, W., Holzmann, H., and Zappa, M.: Glaciermelt of a small basin contributing to runoff under the extreme climate conditions in the summer of 2003, Hydrol. Processes, 23, 1010–1018, https://doi.org/10.1002/hyp.7203, 2009.

Koboltschnig, G. R. and Schöner, W.: The relevance of glacier melt in the water cycle of the Alps: the example of Austria, Hydrol. Earth Syst. Sci., 15, 2039–2048, https://doi.org/10.5194/hess-15-2039-2011, 2011.

Kondo, K., Sugiyama, S., Sakakibara, D., and Fukumoto, S.: Flood events caused by discharge from Qaanaaq Glacier, northwestern Greenland, J. Glaciol., 67, 500–510, https://doi.org/10.1017/jog.2021.3, 2021.

Kronenberg, M., Van Pelt, W., Machguth, H., Fiddes, J., Hoelzle, M., and Pertziger, F.: Long-term firn and mass balance modelling for Abramov Glacier in the data-scarce Pamir Alay, Cryosphere, 16, 5001–5022, https://doi.org/10.5194/tc-16-5001-2022, 2022.

Li, Z., Xiao, Z., and Ling, J.: Impact of extremely warm Tibetan Plateau in spring on the rare rainfall anomaly pattern in the regions west and east to Plateau in late summer 2022, Atmos. Res., 290, 106797, https://doi.org/10.1016/j.atmosres.2023.106797, 2023.

Liang, L., Cuo, L., and Liu, Q.: The energy and mass balance of a continental glacier: Dongkemadi Glacier in central Tibetan Plateau, Sci. Rep., 8, 12788, https://doi.org/10.1038/s41598-018-31228-5, 2018.

(Lisette) Klok, E. J. and Oerlemans, J.: Model study of the spatial distribution of the energy and mass balance of Morteratschgletscher, Switzerland, J. Glaciol., 48, 505–518, https://doi.org/10.3189/172756502781831133, 2002.

Liu, W., Zhang, D., Qin, X., Van Den Broeke, M. R., Jiang, Y., Yang, D., and Ding, M.: Monsoon Clouds Control the Summer Surface Energy Balance on East Rongbuk Glacier (6,523 m Above Sea Level), the Northern of Mt. Qomolangma (Everest), J. Geophys. Res.: Atmos., 126, e2020JD033998, https://doi.org/10.1029/2020JD033998, 2021.

Menounos, B., Huss, M., Marshall, S., Ednie, M., Florentine, C., and Hartl, L.: Glaciers in Western Canada-Conterminous US and Switzerland Experience Unprecedented Mass Loss Over the Last Four Years (2021–2024), Geophys. Res. Lett., 52, e2025GL115235, https://doi.org/10.1029/2025GL115235, 2025.

Mölg, T., Cullen, N. J., Hardy, D. R., Kaser, G., and Klok, L.: Mass balance of a slope glacier on Kilimanjaro and its sensitivity to climate, Int. J. Climatol., 28, 881–892, https://doi.org/10.1002/joc.1589, 2008.

Oerlemans, J. and Knap, W. H.: A 1 year record of global radiation and albedo in the ablation zone of Morteratschgletscher, Switzerland, J. Glaciol., 44, 231–238, https://doi.org/10.3189/S0022143000002574, 1998.

Oerlemans, J., Anderson, B., Hubbard, A., Huybrechts, Ph., Jóhannesson, T., Knap, W. H., Schmeits, M., Stroeven, A. P., Van De Wal, R. S. W., Wallinga, J., and Zuo, Z.: Modelling the response of glaciers to climate warming, Clim. Dyn., 14, 267–274, https://doi.org/10.1007/s003820050222, 1998.

Östin, R. and Andersson, S.: Frost growth parameters in a forced air stream, Int. J. Heat Mass Transfer, 34, 1009–1017, https://doi.org/10.1016/0017-9310(91)90012-4, 1991.

Pu, J., Yao, T., Yang, M., Tian, L., Wang, N., Ageta, Y., and Fujita, K.: Rapid decrease of mass balance observed in the Xiao (Lesser) Dongkemadi Glacier, in the central Tibetan Plateau, Hydrol. Processes, 22, 2953–2958, https://doi.org/10.1002/hyp.6865, 2008.

Raei, E., Nikoo, M. R., AghaKouchak, A., Mazdiyasni, O., and Sadegh, M.: GHWR, a multi-method global heatwave and warm-spell record and toolbox, Sci. Data, 5, 180206, https://doi.org/10.1038/sdata.2018.206, 2018.

Reijmer, C. H. and Hock, R.: Internal accumulation on Storglaciären, Sweden, in a multi-layer snow model coupled to a distributed energy- and mass-balance model, J. Glaciol., 54, 61–72, https://doi.org/10.3189/002214308784409161, 2008.

Shan, B., Verhoest, N. E. C., and De Baets, B.: Identification of compound drought and heatwave events on a daily scale and across four seasons, Hydrol. Earth Syst. Sci., 28, 2065–2080, https://doi.org/10.5194/hess-28-2065-2024, 2024.

Sturm, M., Holmgren, J., König, M., and Morris, K.: The thermal conductivity of seasonal snow, J. Glaciol., 43, 26–41, https://doi.org/10.3189/S0022143000002781, 1997.

Thibert, E., Dkengne Sielenou, P., Vionnet, V., Eckert, N., and Vincent, C.: Causes of Glacier Melt Extremes in the Alps Since 1949, Geophys. Res. Lett., 45, 817–825, https://doi.org/10.1002/2017GL076333, 2018.

Tian, L., Masson-Delmotte, V., Stievenard, M., Yao, T., and Jouzel, J.: Tibetan Plateau summer monsoon northward extent revealed by measurements of water stable isotopes, J. Geophys. Res.: Atmos., 106, 28081–28088, https://doi.org/10.1029/2001JD900186, 2001.

Tian, Y., Ghausi, S. A., Zhang, Y., Zhang, M., Xie, D., Cao, Y., Mei, Y., Wang, G., Zhong, D., and Kleidon, A.: Radiation as the dominant cause of high-temperature extremes on the eastern Tibetan Plateau, Environ. Res. Lett., 18, 074007, https://doi.org/10.1088/1748-9326/acd805, 2023.

Van Tiel, M., Huss, M., Zappa, M., Jonas, T., and Farinotti, D.: Swiss glacier mass loss during the 2022 drought: persistent streamflow contributions amid declining melt water volumes, Hydrol, Earth Syst, Sci, 30, 23–43, https://doi.org/10.5194/hess-30-23-2026, 2026.

Van Pelt, W., Pohjola, V., Pettersson, R., Marchenko, S., Kohler, J., Luks, B., Hagen, J. O., Schuler, T. V., Dunse, T., Noël, B., and Reijmer, C.: A long-term dataset of climatic mass balance, snow conditions, and runoff in Svalbard (1957–2018), Cryosphere, 13, 2259–2280, https://doi.org/10.5194/tc-13-2259-2019, 2019.

Van Pelt, W. J. J., Oerlemans, J., Reijmer, C. H., Pohjola, V. A., Pettersson, R., and Van Angelen, J. H.: Simulating melt, runoff and refreezing on Nordenskiöldbreen, Svalbard, using a coupled snow and energy balance model, Cryosphere, 6, 641–659, https://doi.org/10.5194/tc-6-641-2012, 2012.

Vargo, L. J., Anderson, B. M., Dadić, R., Horgan, H. J., Mackintosh, A. N., King, A. D., and Lorrey, A. M.: Anthropogenic warming forces extreme annual glacier mass loss, Nat. Clim. Change, 10, 856–861, https://doi.org/10.1038/s41558-020-0849-2, 2020.

Voordendag, A., Prinz, R., Schuster, L., and Kaser, G.: Brief communication: The Glacier Loss Day as an indicator of a record-breaking negative glacier mass balance in 2022, Cryosphere, 17, 3661–3665, https://doi.org/10.5194/tc-17-3661-2023, 2023.

Wang, Z., Duan, A., Yang, S., and Ullah, K.: Atmospheric moisture budget and its regulation on the variability of summer precipitation over the Tibetan Plateau, J. Geophys. Res.: Atmos., 122, 614–630, https://doi.org/10.1002/2016JD025515, 2017.

Wei, Y. and Yu, H.: The Interdecadal Weakening of the Relationship Between Indian Ocean Sea Surface Temperature and Summer Precipitation in Central Asia, Geophys. Res. Lett., 51, e2023GL107371, https://doi.org/10.1029/2023GL107371, 2024.

Xu, C., Li, H., Wang, F., Li, Z., Zhou, P., and Liu, S.: Heatwaves in summer 2022 forces substantial mass loss for Urumqi Glacier No. 1, China, J. Glaciol., 70, e77, https://doi.org/10.1017/jog.2024.4, 2024.

Yan, R., Wang, X., Wang, J., Tan, J., and Ju, W.: Warm Early Summer Compensated Reduction in Photosynthesis Caused by 2022 Late Summer Extreme Drought Over the Tibetan Plateau, J. Geophys. Res.: Biogeosci., 129, e2023JG007859, https://doi.org/10.1029/2023JG007859, 2024.

Yao, T., Thompson, L., Yang, W., Yu, W., Gao, Y., Guo, X., Yang, X., Duan, K., Zhao, H., Xu, B., Pu, J., Lu, A., Xiang, Y., Kattel, D. B., and Joswiak, D.: Different glacier status with atmospheric circulations in Tibetan Plateau and surroundings, Nat. Clim. Change, 2, 663–667, https://doi.org/10.1038/nclimate1580, 2012.

Yao, T., Masson-Delmotte, V., Gao, J., Yu, W., Yang, X., Risi, C., Sturm, C., Werner, M., Zhao, H., He, Y., Ren, W., Tian, L., Shi, C., and Hou, S.: A review of climatic controls on δ^{18} O in

precipitation over the Tibetan Plateau: Observations and simulations, Rev. Geophys., 51, 525–548, https://doi.org/10.1002/rog.20023, 2013.

Yao, T., Bolch, T., Chen, D., Gao, J., Immerzeel, W., Piao, S., Su, F., Thompson, L., Wada, Y., Wang, L., Wang, T., Wu, G., Xu, B., Yang, W., Zhang, G., and Zhao, P.: The imbalance of the Asian water tower, Nat. Rev. Earth Environ., 3, 618–632, https://doi.org/10.1038/s43017-022-00299-4, 2022.

Yen, Y.: Review of thermal properties of snow, ice and sea ice, Tech. rep., DTIC Document, 1981.

Zhang, T., Deng, Y., Chen, J., Yang, S., and Dai, Y.: An energetics tale of the 2022 mega-heatwave over central-eastern China, npj Clim. Atmos. Sci., 6, 162, https://doi.org/10.1038/s41612-023-00490-4, 2023.

Zhou, B., Zhai, P., and Liao, Z.: Bivariate attribution of the compound hot and dry summer of 2022 on the Tibetan Plateau, Sci. China Earth Sci., 67, 2122–2136, https://doi.org/10.1007/s11430-023-1320-y, 2024.

Zhu, F., Zhu, M., Yang, W., Wang, Z., Guo, Y., and Yao, T.: Drivers of the Extreme Early Spring Glacier Melt of 2022 on the Central Tibetan Plateau, Earth Space Sci., 11, https://doi.org/10.1029/2023ea003297, 2024a.

Zhu, F., Zhu, M., Guo, Y., and Yao, T.: Observation and Simulation of Runoff During an Extreme Heatwave in a Glacial Basin on the Central Tibetan Plateau, Hydrol. Processes, 38, e70014, https://doi.org/10.1002/hyp.70014, 2024b.

Zhu, F., Yao, T.-D., Zhu, M.-L., An, L., Wang, P., Huang, G.-F., and Hu, Z.-F.: The role of mid-latitude zonal wind anomalies in extreme glacier mass loss on central Tibetan Plateau, Adv. Clim. Change Res., https://doi.org/10.1016/j.accre.2026.03.010, 2026a.

Zhu, M., Yao, T., Yang, W., Xu, B., Wu, G., and Wang, X.: Differences in mass balance behavior for three glaciers from different climatic regions on the Tibetan Plateau, Clim. Dyn., 50, 3457–3484, https://doi.org/10.1007/s00382-017-3817-4, 2018.

Zhu, M., Thompson, L. G., Zhao, H., Yao, T., Yang, W., and Jin, S.: Influence of atmospheric circulation on glacier mass balance in western Tibet: an analysis based on observations and modeling, J. Clim., 1–55, https://doi.org/10.1175/JCLI-D-20-0988.1, 2021.

Zhu, M., Yao, T., Thompson, L. G., Wang, S., Yang, W., and Zhao, H.: What induces the spatiotemporal variability of glacier mass balance across the Qilian Mountains, Clim Dyn, 59, 3555–3577, https://doi.org/10.1007/s00382-022-06283-4, 2022a.

Zhu, M., Yao, T., Yang, W., Wu, G., Li, S., Zhao, H., and Thompson, L. G.: Possible Causes of Anomalous Glacier Mass Balance in the Western Kunlun Mountains, J. Geophys. Res.: Atmos., 127, e2021JD035705, https://doi.org/10.1029/2021JD035705, 2022b.

Zhu, M., Yao, T., Thompson, L. G., Yang, W., Zhu, F., Lin, D., Zhong, Z.-P., Zhao, H., Zhang, X., and Li, S.: Linking northeastern indian subcontinental high temperature to extreme glacier mass loss on the south-central Tibetan Plateau, J. Geophys. Res.: Atmos., 131, e2025JD045031, https://doi.org/10.1029/2025JD045031, 2026b.